

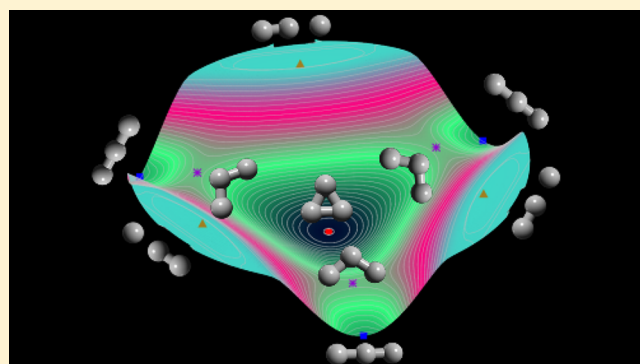
Accurate CHIPR Potential Energy Surface for the Lowest Triplet State of C_3

C.M.R. Rocha[†] and A.J.C. Varandas^{*,‡,†}[†]Coimbra Chemistry Centre and Chemistry Department, University of Coimbra, 3004-535 Coimbra, Portugal[‡]School of Physics and Physical Engineering, Qufu Normal University, Qufu 273165, P. R. China

Supporting Information

ABSTRACT: We report the first global ab initio-based potential energy surface (PES) for ground-state triplet $C_3(^3A')$ based on accurate energies extrapolated to the complete basis set (CBS) limit, and using the combined-hyperbolic-inverse-power-representation method for the analytical modeling. By relying on a cost-effective CBS(D,T) protocol, we ensure that the final form reproduces all topographical features of the PES, including its cyclic-linear isomerization barrier, with CBS(5,6)-quality. To partially account for the incompleteness of the N -electron basis and other minor effects, the available accurate experimental data on the relevant diatomics were used to obtain direct-fit curves that replace the theoretical ones in the many-body expansion.

Besides describing properly long-range interactions at all asymptotic channels and permutational symmetry by built-in construction, the PES reported here reproduces the proper exothermicities at dissociation regions as well as the spectroscopy of the diatomic fragments. Bound vibrational state calculations in both linear and cyclic isomers have also been carried out, unveiling a good match of the available data on $C_3(\tilde{a}^3\Pi_u)$, while assisting with IR band positions for $C_3(^3A'_2)$ that may serve as a guide for its laboratory and astronomical detection.



1. INTRODUCTION

Carbon clusters represent a unique and challenging class of molecules with broad implications in chemistry and astrophysics.¹ Along with C_2 , the carbon trimer (C_3) is one of the most studied among its family and still attracts much interest of both experimentalists and theorists alike for a number of reasons:²

- (i) C_3 is known to appear in a myriad of astronomical objects, notably in circumstellar envelopes of C -rich stars,³ comets,⁴ and in various regions of the interstellar medium.^{5–7} Yet, C_3 formation/destruction reactions are regarded as major routes governing carbon chain abundances in dark clouds^{8,9} and chemical modeling of (exo)planetary atmospheres.^{10,11}
- (ii) C_3 is the dominant vapor species over graphite above ≈ 2000 K,¹² a fact that also underpins its importance in combustion environments and as a potential precursor for soot formation in flames.¹³
- (iii) C_3 is a prototypical example of floppy linear molecules: its ground electronic state, $\tilde{X}^1\Sigma_g^+$, has an unusually low bending frequency of $\nu_2 \approx 63$ cm^{−1} (the corresponding harmonic w_2 goes as low as 43 cm^{−1}).¹⁴ Yet, the expected high vibrational state populations and their delocalization over large regions of its potential energy surface (PES)¹⁵ make C_3 intramolecular motion highly

anharmonic and lying at the borderlines of spectroscopy and chemical dynamics.¹⁴

- (iv) Linear C_3 is a well-known example of a Renner–Teller (RT) system:^{16–19} its excited $\tilde{a}^3\Pi_w$,^{18,19} $\tilde{b}^3\Pi_g$,^{18,19,18,19} $\tilde{A}^1\Pi_w$,¹⁶ and even $\tilde{D}^1\Delta_g$ ¹⁷ states are among the most studied prototypes due to strong vibronic interactions on bending.^{16–19}
- (v) C_3 is also part of a select group of triatomics, the small linear parameter Jahn–Teller (JT) molecules,^{20,21} wherein combined JT plus pseudo-JT vibronic couplings dictate the topology of their PESs near D_{3h} symmetrical arrangements. As shown for C_3 ,^{20,21} such effects originate four conical intersections involving the first two $^1A'$ states, with loci that evolve in a rather intricate way.²¹

All of the above features make carbon trimer a complicated (see Figure 1) but fascinating molecule, whose study unavoidably links several (multidisciplinary) branches of science.² Although a flurry of experimental/theoretical studies have been advocated in characterizing singlet states of C_3 (notably, the ground $^1\Sigma_g^+$ and the first excited singlet $^1\Pi_w$ involved in its well-known cometary or Swing band system^{1,2}),

Received: April 5, 2019

Revised: June 3, 2019

Published: June 11, 2019

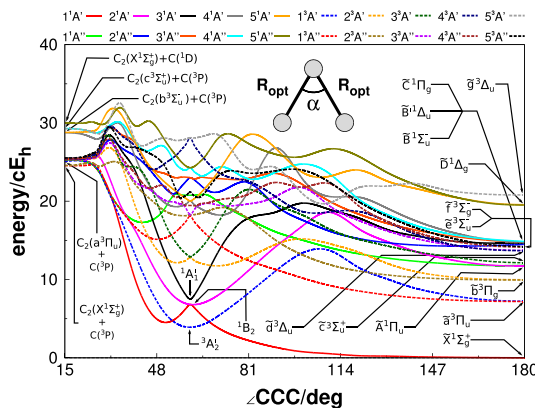


Figure 1. Optimized bending profiles for ground and low-lying excited singlet and triplet states of C_3 as obtained by performing state-averaged CASSCF(12,12)/AVTZ calculations involving five electronic states of A' (A'') symmetry (in the C_s symmetry point group). The key shows the irreducible representations for each electronic state. Also, shown are the associated correlations for linear geometries using $D_{\infty h}$ symmetry, and the corresponding dissociation limits. Only single-point calculations have been performed using previously optimized ground-state geometries.²²

relatively few studies were devoted to its triplet manifold.^{18,19,23–35}

To the best of our knowledge, the first experimental evidence on triplet C_3 was reported by Weltner and McLeod,²³ while investigating carbon vapor trapped in rare-gas matrices. The authors observed a strong phosphorescence emission at $\approx 17\,000\text{ cm}^{-1}$ and attributed it to the spin-forbidden $^3\Pi_u \rightarrow \tilde{X}$

$^1\Sigma_g^+$ transition of C_3 . Bondybey and English²⁴ performed a detailed study of this band and confirmed its upper state as the $\tilde{a}\ ^3\Pi_u$. Moreover, they suggested that intersystem crossing into the triplet manifold occurs from the (0,0,0) level of $\tilde{A}\ ^1\Pi_u$, lying at $\approx 25\,000\text{ cm}^{-1}$ above the ground $^1\Sigma_g^+$ state.²⁴

The first rotationally resolved gas-phase spectrum involving triplet states of C_3 was recorded by Sasada et al.²⁵ They observed a band at $\approx 6500\text{ cm}^{-1}$ and assigned it to the (0,0,0)–(0,0,0) transition of $\tilde{b}\ ^3\Pi_g$ – $\tilde{a}\ ^3\Pi_u$. From the rotational constants so obtained, they also provided bond lengths r_0 for both the upper (2.430 a_0) and lower (2.453 a_0) states. The proximity of the r_0 value for $\tilde{a}\ ^3\Pi_u$ with that of $\tilde{A}\ ^1\Pi_u$ (2.466 a_0) has been suggested²⁵ as implying that they arise from the same electron configuration (... $1\pi_u^4 4\sigma_g^2 3\sigma_u^1 1\pi_g^1$). In turn, Smith et al.²⁶ performed double-resonance spectroscopy of C_3 trapped in rare-gas matrices and reported the first estimates of the fundamental stretching frequencies for $\tilde{a}\ ^3\Pi_u$. The corresponding gas-phase values were given later by Hwang et al.²⁷ The first rotationally resolved gas-phase spectrum arising from excited bending vibrations in the transition $\tilde{b}\ ^3\Pi_g \rightarrow \tilde{a}\ ^3\Pi_u$ was reported by Tokaryk and co-workers.^{18,19} As they remarked, the structure of the band is rather intricate due to the spin-orbit and RT effects. From the analysis of the spectrum, they determined Renner parameters, which were considered as large as in the case of $\tilde{A}\ ^1\Pi_u$ ($\epsilon = +0.537$).^{18,19} Such values allowed an estimate (non-vibronic) of harmonic frequencies (w_2) as 542.3 cm^{-1} for $\tilde{a}\ ^3\Pi_u$ and 392.4 cm^{-1} for $\tilde{b}\ ^3\Pi_g$. More recently, Sych et al.³⁵ employed perturbation-facilitated two-color resonant four-wave-mixing spectroscopy to access the (dark) triplet states of C_3 from the $^1\Sigma_g^+$ ground state. They observed

that the newly found $^3\Pi_g$ vibronic level could perhaps be assigned to the hitherto unidentified $^3\Delta_u$ state.

Apart from experimental studies, a number of quantum calculations have been carried out to examine the trimer triplet manifold.^{28–34} It turns out that the former were mostly concerned with the characterization of linear structures and hence no experimental data is available thus far for other structural forms.

Early work by Williams²⁸ and Perić-Radić et al.,²⁹ using the equation of motion and multireference configuration interaction (MRCI) methods, respectively, is primarily devoted to the electronic spectra of C_3 and the Weltner–McLeod²³ tentative assignment of the $\tilde{a}\ ^3\Pi_u \rightarrow \tilde{X}\ ^1\Sigma_g^+$ band. Perić-Radić et al. also reported cuts along normal coordinates for triplet linear structures, unraveling the large RT splitting of the $\tilde{a}\ ^3\Pi_u(^3B_1, ^3A_1)$ and $\tilde{b}\ ^3\Pi_g(^3A_2, ^3B_2)$ degenerate components on bending.²⁹ In turn, Whiteside et al.³⁰ employed fourth-order Möller–Plesset perturbation theory (MP4) and the 6-31G* basis set to characterize cyclic structures of the trimer. They were the first to note that the cyclic D_{3h} structure is a minimum (with $e^{1/2}$ valence configuration) on the ground-state triplet PES of C_3 , which correlates with $^3A'_2$.²⁰ It lies $\approx 102.1\text{ kJ mol}^{-1}$ above the $^1\Sigma_g^+$ global minimum, and³² 129.3 kJ mol^{-1} below the linear equilibrium geometry of $\tilde{a}\ ^3\Pi_u$; thence, it is the first excited state of C_3 . Fueno and Taniguchi³² performed complete active space self-consistent field (CASSCF) and MRCI/6-311+G* calculations on the cyclization path of some low-lying excited trimeric states. They noted that the isomerization between the cyclic $^3A'_2$ and $\tilde{a}\ ^3\Pi_u$ forms occurs via a $C_s(^3A')$ transition state, with a classical barrier height of 272.0 kJ mol^{-1} . They further noted the presence of a conical intersection between the 3A_1 and 3B_2 RT components, which originate from $\tilde{a}\ ^3\Pi_u(^3B_1, ^3A_1)$ and $\tilde{b}\ ^3\Pi_g(^3A_2, ^3B_2)$, correlate with the same $^3A'$ symmetry species in C_s .³²

Mebel and Kaiser³³ examined ab initio the possible sources of the formation of $C_3(X\ ^1\Sigma_g^+)$ and $C_3(^3A'_2)$ in cold interstellar environments. Using CCSD(T)/6-311+G(3df,2p), they suggested³³ that the (barrierless) reactions of $CH(X\ ^2\Pi) + C_2(X\ ^1\Sigma_g^+)$ and $C(^3P) + C_2H(X\ ^2\Sigma^+)$ (which involve the C_3H intermediate) represent facile neutral–neutral (exothermic) pathways yielding carbon trimer species. Furthermore, they concluded that $C_3(^3A'_2)$ is readily formed through the fragmentation of cyclic C_3H and hence acknowledged for the first time its relevance in the interstellar medium. Besides the cyclic form, we should note the previous association of the $\tilde{a}\ ^3\Pi_u \rightarrow \tilde{X}\ ^1\Sigma_g^+$ transition to the (enigmatic) Red Rectangle bands⁷ and also the expected relevance of $C_3(\tilde{a}\ ^3\Pi_u)$ to the formation of (interstellar) C_3H in C_2H_2 -rich environments.³⁶ All of the above features, together with the fact that relatively few data are available on triplet C_3 [practically none for the case of $C_3(^3A'_2)$], render this system a tempting target for further studies.

The purpose of this work is to report the first global PES for ground-state triplet C_3 . It correlates with the $\tilde{a}\ ^3\Pi_u$ state at linear geometries and $^3A'_2$ for equilateral triangular ones. The PES will be based on accurate ab initio energies extrapolated to the complete basis set (CBS) limit, which is then modeled analytically using the combined-hyperbolic-inverse-power-representation (CHIPR) method.^{37–39} The paper is structured as follows. **Section 2** deals with the ab initio calculations and CBS extrapolation scheme. The details of the modeling are given in **Section 3**, whereas the topographical features of the

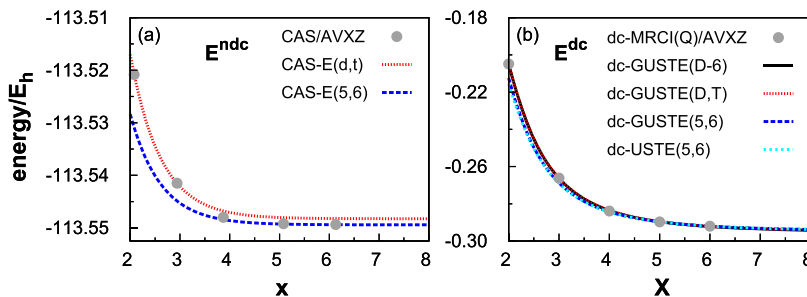


Figure 2. Graphical representation of the absolute energies obtained from the raw ab initio MRCI(Q)/AVXZ calculations and extrapolation formulas of eqs 2 and 3 for the global minimum of triplet C_3 . In the abscissa, x and X represent the hierarchical and cardinal numbers of the basis sets, respectively.

Table 1. Absolute Energies Obtained from the Extrapolation Formulas of Equations 2 and 3 for $\text{Min}(D_{3h})$; See Table S1 for an Extended Version

method ^a	E^{ndc} (E_h)	method ^a	E^{dc} (E_h)	$E^{\text{ndc+dc}}$ (E_h)
CAS-E(d,t)	-113.548260	dc-USTE(D,T)	-0.297054	-113.845315
CAS-E($S,6$)	-113.549420	dc-USTE($S,6$)	-0.295027	-113.844447
		dc-GUSTE(D,T)	-0.295417	-113.843678
		dc-GUSTE($S,6$)	-0.295019	-113.844439

^aThis work. Energies calculated at the CAS/AVTZ global minimum of triplet C_3 with structural parameters $R_1 = R_2 = 2.629 \text{ \AA}$ and $\angle CCC = 60.0^\circ$.

final CHIPR PES are discussed in Section 4. The quality of the latter is further judged via spectroscopic calculations in Section 5. Some conclusions are gathered in Section 6.

2. AB INITIO CALCULATIONS AND CBS EXTRAPOLATION

The calculations reported in the present work have been done at MRCI level of theory including the Davidson correction [MRCI(Q)] and full-valence CASSCF [CASSCF(12,12) or CAS] as reference.⁴⁰ The active space includes all valence orbitals that correlate with 2s and 2p atomic shells in a total of 12 molecular orbitals (and 12 electrons). All single and double excitations out of the CAS space were included in the internally contracted MRCI wave function, using one reference state and the $C_s(A')$ symmetry point group. The aug-cc-pVQZ [AVXZ($X = D - 6$)] Dunning-type basis sets^{41,42} were employed, with all calculations performed with MOLPRO.⁴³ The ab initio energies so obtained were subsequently extrapolated to the CBS limit. Due to the distinct (asymptotic) convergence rates, the CBS extrapolations were performed separately for the nondynamical (ndc) and dynamical (dc) correlations⁴⁴

$$E_{\infty}^{\text{CBS}}(\mathbf{R}) = E_{\infty}^{\text{CAS}}(\mathbf{R}) + E_{\infty}^{\text{dc}}(\mathbf{R}) \quad (1)$$

where \mathbf{R} is a collective coordinate.

For the ndc, a two-point extrapolation protocol developed in our group⁴⁶ has been utilized

$$E_X^{\text{CAS}}(\mathbf{R}) = E_{\infty}^{\text{CAS}}(\mathbf{R}) + A e^{-1.63x} \quad (2)$$

where $x = d$ (2.08), t (2.94), q (3.87), p (5.08), and h (6.13) are hierarchical numbers^{47,48} that parallel the traditional $X = D, T, Q, S, 6$ cardinal ones and $E_{\infty}^{\text{CAS}}(\mathbf{R})$ [hereinafter denoted CAS-exponential or $\text{CAS-E}(x, x_i)$ ⁴⁶] and A are parameters obtained from the raw CAS/AVXZ ndc energies.

The extrapolated dc contribution [$E_{\infty}^{\text{dc}}(\mathbf{R})$] has in turn been obtained from either Varandas' uniform singlet- and triplet-pair extrapolation (USTE)⁴⁵ or generalized USTE (GUSTE)⁴⁹ protocols. They both hinge on the following dual-level law⁴⁴

$$E_X^{\text{dc}}(\mathbf{R}) = E_{\infty}^{\text{dc}}(\mathbf{R}) + \frac{A_3}{(X - 3/8)^3} + \frac{\eta A_5^{\circ} + c A_3^{5/4}}{(X - 3/8)^5} \quad (3)$$

where A_5° and c are universal-type parameters⁴⁵ and $E_{\infty}^{\text{dc}}(\mathbf{R})$ [referred to as dc-USTE(X_i, X_j) or dc-GUSTE(X_i, X_j)] and A_3 are obtained from the raw MRCI(Q)/AVXZ dc energies. Note that, the scaling factor η equals 1 in USTE while being system-dependent in GUSTE: it is optimized to warrant the best performance.⁴⁹ Indeed, based on the premise that η is invariant over the whole configuration space of the molecule (as in the correlation scaling approach^{50,51}), its value is calibrated from a single (or a few) pivotal geometry(ies) such as to mimic any desired result and/or allow the extrapolation formula to mimic its best CBS estimate. Within the same spirit of refs 49 and 50, we choose η from the requirement that the GUSTE protocol (eq 3) optimally fits the calculated dc-MRCI(Q)/AVXZ ($X = D - 6$) energies at the CAS/AVTZ global minimum ($R_1 = R_2 = 2.629 \text{ \AA}$ and $\angle CCC = 60.0^\circ$) of the triplet ground-state C_3 PES, hereafter denoted $\text{Min}(D_{3h})$. The GUSTE curve and all energies obtained with the extrapolation formulas 2 and 3 are displayed in Figure 2 and gathered for completeness in Table 1; see also the Supporting Information (SI). Also shown in Table 2 are the optimum parameters of eq 3. Notably, the

Table 2. GUSTE Extrapolation Parameters

A_5° (E_h) ^a	c ($E_h^{-1/4}$) ^a	η ^b
0.0037685459	-1.1784771300	11.4147751928

^aRef 45. ^bThis work. Unitless.

extrapolated dc energy from GUSTE with the smallest affordable basis sets, i.e., dc-GUSTE(D,T) and $\eta \approx 11$, reproduces nearly exactly the corresponding dc-GUSTE($S,6$) and dc-USTE($S,6$) energies (see Table 1). In fact, the two sets of results so obtained are nearly identical, which evinces the robustness of the GUSTE method. Indeed, the error amounts to only 0.1% of the total CBS dc energy ($\sim 0.4 \text{ mE}_h$), which is

about the highest accuracy one possibly can get from raw energies of the lowest $X = D, T$ hierarchical rungs.

Figure 2a and **Table 1** show also the feasibility of extrapolating the ndc components via **eq 2** using the present (D, T) protocol. As seen, the CAS-E(d, t) limit underestimates the CAS-E($S, 6$) ndc energy by $\approx 1 \text{ mE}_h$ (0.001%). Moreover, a closer look at **Table S1** unravels the faster asymptotic behavior of the ndc component toward the CBS limit that appears to be nearly converged already at the AV6Z level. This further supports the energy split in **eq 1**.⁴⁴ As a final remark, we should note that the total CBS energy obtained by summing the CAS-E(d, t) and dc-GUSTE(D, T) components [referred to as MRCI(Q)/GUSTE(D, T) or GUSTE(D, T)] underestimates the best estimate of the CBS limit by 0.8 mE_h (0.0007%) at the global minimum, and hopefully elsewhere.

With the GUSTE(D, T) protocol in mind, the calibration of the global PES has therefore been carried out by performing calculations at the MRCI(Q)/AVXZ ($X = D, T$) level. A total of 5999 symmetry unrelated grid points were judiciously chosen for the purpose of mapping the C + C₂ channel: $1.8 \leq R_1/a_0 \leq 3.5$, $1.5 \leq R_2/a_0 \leq 10.0$, and $60.0 \leq \angle \text{CCC}/\text{deg} \leq 180.0$, where R_1 , R_2 , and $\angle \text{CCC}$ are valence coordinates.¹⁵

3. CHIPR PES

3.1. General Aspects. In the CHIPR method of Varandas,^{37,38} the PES of a triatomic molecule assumes the many-body expansion (MBE)¹⁵ form

$$V(\mathbf{R}) = V_S^{(1)} + V_S^{(2)}(\mathbf{R}) + V_S^{(3)}(\mathbf{R}) \quad (4)$$

where $V_S^{(1)}$ is the sum of (pseudo-) one-body fragments, $V_S^{(2)}(\mathbf{R}) = \sum_{i=1}^3 V_i^{(2)}(R_i)$ is the sum of all two-body potentials, and the last term is the three-body interaction; $\mathbf{R} = \{R_1, R_2, R_3\}$ is the set of bond distances. Since C₃(³A') dissociates adiabatically to C(³P) + C(³P) + C(³P), $V_S^{(1)} = 0$, with the zero of energy being the three isolated ground-state C atoms.¹⁵

As in MBE¹⁵ and double many-body expansion (DMBE)⁵² theories, $V_S^{(n)}(\mathbf{R})$ must account for the permutational symmetry of the full molecular aggregate as implied by the subindex S. For the two-body case, this condition is naturally warranted whenever all (three) diatomic potentials are introduced into the summation $V_S^{(2)}(\mathbf{R})$. Yet, for higher-order terms ($n = 3$ in this case), permutation invariance is generally ensured by built-in construction via the use of symmetrized sums of monomials (see below).³⁹ Note further that, as in MBE/DMBE, any of the n -body terms in **eq 4** should vanish when any atom is far from the ($n - 1$)-atom aggregate.

For a N -atom system, the general form of the various CHIPR n -body terms are written as^{37,38}

$$V_S^{(n)}(\mathbf{R}^n) = \sum_{i_1=0, \dots, i_\tau}^L C_{i_1, \dots, i_\tau} \prod_{p=1}^\tau y_p^{i_p} \quad (5)$$

where C_{i_1, \dots, i_τ} are expansion coefficients of an L th-order polynomial, with the y_p 's representing the set of $p = 1, 2, \dots$ transformed (τ) coordinates relative to some reference geometry; τ is the total number of $n(n - 1)/2$ internal (independent) degrees of freedom on which the subset \mathbf{R}^n depends. As in electronic structure theory,⁴⁰ each y_p in **eq 5** is

in turn expanded via a distributed-origin contracted basis set^{37,38}

$$y_p = \sum_{\alpha=1}^M c_\alpha \phi_{p,\alpha} \quad (6)$$

where $\phi_{p,\alpha}$ assumes one of two following convenient forms:

- (i) if long-range terms are ignored, the basis functions are set up as³⁷

$$\phi_{p,\alpha}^{[1]} = \operatorname{sech}^{\eta_\alpha}(\gamma_{p,\alpha} \rho_{p,\alpha}) \quad (7)$$

- (ii) if long-range energies are envisaged, the preference is³⁷

$$\phi_{p,\alpha}^{[2]} = \left[\frac{\tanh(\beta_\alpha R_p)}{R_p} \right]^{\sigma_\alpha} \operatorname{sech}^{\eta_\alpha}(\gamma_{p,\alpha} \rho_{p,\alpha}) \quad (8)$$

In the above equations, $\rho_{p,\alpha} = R_p - R_{p,\alpha}^{\text{ref}}$ is the deviation of R_p from the primitive's origin $R_{p,\alpha}^{\text{ref}}$ and $\gamma_{p,\alpha}$ are nonlinear parameters. Although the quantities η_α , σ_α , and β_α can be optimized at will, they are usually fixed for convenience as $\eta_\alpha \equiv \eta = 1$, $\sigma_\alpha \equiv \sigma = 6$, and $\beta_\alpha \equiv \beta = 1/5$.^{37,38} Of course, any combination of the above basis can also be advocated in devising flexible and suitable coordinate transformations, which are actually the approaches followed here (see later). Finally, to reduce linear dependencies, the distributed origins ($R_{p,\alpha}^{\text{ref}}$) of the various basis functions defined in **eq 6** are assumed to be related by

$$R_{p,\alpha}^{\text{ref}} = \zeta (R_p^{\text{ref}})^{\alpha-1} \quad (9)$$

where ζ and R_p^{ref} are constants, and α defines the index of each primitive function in **eq 6**. As noted elsewhere,³⁷ the above two-parameter relation resembles the even-tempered algorithm for one-electron basis sets.

In the following, we specialize in the title system and discuss the explicit functional forms of the two- and three-body terms utilized here for modeling the ground-state triplet PES of C₃. For completeness, we also provide as SI all required formulas to generate analytic gradients for a general CHIPR triatomic PES.

3.2. Two-Body Terms. According to the spin-spatial Wigner–Witmer rules,⁵³ the dissociation of C₃ in its triplet ground state correlates as follows

$$C_3(^3A') \Rightarrow \begin{cases} C_2(X \ ^1\Sigma_g^+) + C(^3P_g) & R < R_{c_{12}} \\ C_2(a \ ^3\Pi_u) + C(^3P_g) & R_{c_{12}} < R < R_{c_{23}} \\ C_2(b \ ^3\Sigma_g^-) + C(^3P_g) & R > R_{c_{23}} \end{cases} \quad (10)$$

where R is the diatomic coordinate (e.g., for a geometry of C_{2v} symmetry: $R = R_i$ and $R_j = R_k \neq \infty$), $R_{c_{12}} \approx 2.447 \text{ a}_0$, and $R_{c_{23}} \approx 3.170 \text{ a}_0$. **Figure 3** shows the potential energy for a cut along the above bond of the triatomic when the third C atom is far away (but at a finite distance) from the other two. This is shown by the solid black dots and compared with the potential curves for the various electronic states of the isolated C₂. Clearly, the points follow the curves of three distinct diatomic states along the bond stretching coordinate. This may be rationalized from **Table 3**, which shows all possible states of C₃ arising from the C + C₂ interaction in C_s symmetry. As seen, the diatomic states in **eq 10** are uncoupled in D_{∞h} symmetry

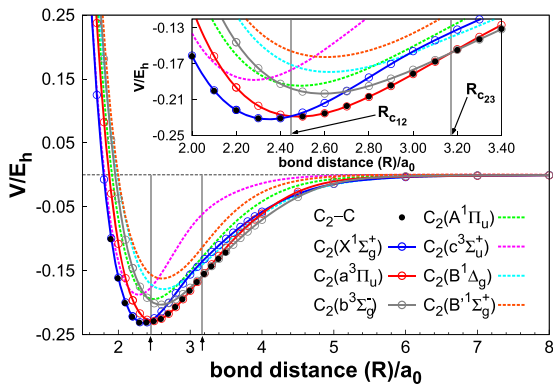


Figure 3. Potential energy curves for various electronic states of the C_2 molecule calculated at the GUSTE(D,T) level. Shown by solid lines are the fitted diagonal terms in eq 11 for the $\text{C}_2(\text{X } ^1\text{\Sigma}_g^+)$, $\text{C}_2(\text{a } ^3\text{\Pi}_u)$, and $\text{C}_2(\text{b } ^3\text{\Sigma}_g^-)$ states, as well as by black solid dots the GUSTE(D,T) points calculated at the $\text{C} + \text{C}_2$ asymptote for fixed values of $r = 20.0 \text{ a}_0$ and $\phi = 90.0^\circ$; R , r , and ϕ are Jacobi coordinates.

Table 3. Final C_3 States Arising from Those of the Isolated $\text{C} + \text{C}_2$ Fragments in C_s Symmetry

atom + diatom	triatom	
	C_s	C_s
$^1\text{\Sigma}_g^+ \otimes ^3\text{P}_g$	$^1(\text{A}') \otimes ^3(\text{A}' + 2\text{A}'')$	$^3(\text{A}' + 2\text{A}'')$
$^3\text{\Pi}_u \otimes ^3\text{P}_g$	$^3(\text{A}' + \text{A}'') \otimes ^3(\text{A}' + 2\text{A}'')$	$^{1,3,5}(3\text{A}' + 3\text{A}'')$
$^3\text{\Sigma}_g^- \otimes ^3\text{P}_g$	$^3(\text{A}'') \otimes ^3(\text{A}' + 2\text{A}'')$	$^{1,3,5}(2\text{A}' + \text{A}'')$

(due to distinct spin/spatial symmetries), but their resolution into C_s and subsequent coupling with $\text{C}(^3\text{P}_g)$ leads to at least three low-energy asymptotic $^3\text{A}'$ states that interact for finite atom + diatom separations. For a similar modeling problem in $\text{HN}_2(^2\text{A}')$, Mota et al.⁵⁴ employed a switching-function formalism in configuration space. Instead, we adopt here pseudo-adiabatic curves that arise from the diagonalization of the following 3×3 symmetric potential matrix^{55–57}

$$\mathcal{H}_e = \begin{pmatrix} \mathcal{V}_{11}^{(2)}(R) & \mathcal{V}_{12}^{(2)}(R) & \mathcal{V}_{13}^{(2)}(R) \\ \mathcal{V}_{12}^{(2)}(R) & \mathcal{V}_{22}^{(2)}(R) & \mathcal{V}_{23}^{(2)}(R) \\ \mathcal{V}_{13}^{(2)}(R) & \mathcal{V}_{23}^{(2)}(R) & \mathcal{V}_{33}^{(2)}(R) \end{pmatrix} \quad (11)$$

where the $\mathcal{V}_{ii}^{(2)}$ represents the pure $\text{C}_2(\text{X } ^1\text{\Sigma}_g^+)$, $\text{C}_2(\text{a } ^3\text{\Pi}_u)$, and $\text{C}_2(\text{b } ^3\text{\Sigma}_g^-)$ diatomic states shown in Figures 3 and 5, and $\mathcal{V}_{ij}^{(2)}$ the corresponding coupling terms. The modeling of the $\mathcal{V}_{ii}^{(2)}$'s is accomplished using eq 5 once the Coulombic interaction required for the two-body case is included^{37,38}

$$\mathcal{V}_{ii}^{(2)}(R) = \frac{Z_A Z_B}{R} \sum_{k=1}^L C_k y^k \quad (12)$$

where Z_A and Z_B denote the nuclear charges of atoms A and B. In turn, the off-diagonal terms in eq 11 can be conveniently represented by⁵⁷

$$\mathcal{V}_{ij}^{(2)}(R) = \frac{\tilde{A}_{ij} \tilde{a}_{ij}}{2} \operatorname{sech}[\tilde{a}_{ij}(R - R_{c_{ij}})] \quad (13)$$

where \tilde{A}_{ij} and \tilde{a}_{ij} are parameters, and $R_{c_{ij}}$ defines the crossings between the states i and j .

The two-step procedure employed for calibrating eq 11 is similar to the one used in previous work.^{54–56} First, the diatomic curves for states $^1\text{\Sigma}_g^+$, $^3\text{\Pi}_u$, and $^3\text{\Sigma}_g^-$ were obtained using 37 ab initio GUSTE(D,T) energies each, and the CHIPR form in eq 12. The optimum parameters were then fixed, and the off-diagonal couplings $\mathcal{V}_{ij}^{(2)}$ (eq 13) calibrated such that the lowest eigenvalue of \mathcal{H}_e (diagonalized via Jacobi method⁵⁸) fits the adiabatic GUSTE(D,T) energies at the $\text{C} + \text{C}_2$ asymptote. Note that all minimizations employed the nonlinear Levenberg–Marquardt^{59,60} method.⁶¹ Such diagonal, $\mathcal{V}_{ii}^{(2)}$, and pseudo-adiabatic, $V_i^{(2)}$, curves are in Figures 4 and 5; see attributes in Table 4. The numerical coefficients in eq 11 and other contributions to the CHIPR PES are given as the SI.

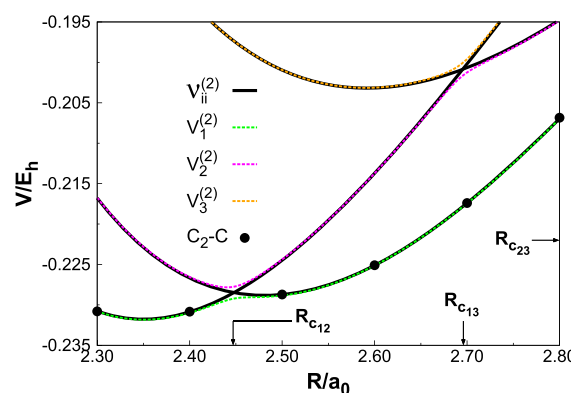


Figure 4. Lowest pseudo-adiabatic diatomic states arising from the diagonalization of eq 11. The solid black lines represent the fitted diagonal terms, while the black solid dots indicate the ab initio GUSTE(D,T) energies calculated at the $\text{C} + \text{C}_2$ asymptote.

Clearly, the CHIPR method reproduces accurately the calculated GUSTE(D,T) energies: root-mean-square deviation (rmsd) of 20.3, 2.6, and 5.3 cm^{-1} for $^1\text{\Sigma}_g^+$, $^3\text{\Pi}_u$, and $^3\text{\Sigma}_g^-$ states, in the same order. Not surprisingly, the somewhat larger deviation for $\text{C}_2(\text{X } ^1\text{\Sigma}_g^+)$ is due to the avoided crossing with the next $\text{B}' ^1\text{\Sigma}_g^+$ state at $R_c \approx 3.0 \text{ a}_0$ (Figure 3, and shaded area in Figure 5), a feature rather difficult to mimic via a single curve fit. Indeed, as demonstrated elsewhere,^{55,56,65,66} the adiabatic ground-state curve itself is only accurately represented as the lowest eigenvalue of a 2×2 potential matrix. Because this avoided crossing is out of the range spanned by $V_1^{(2)} \equiv V^{(2)}$ (see Figure 4), no additional effort has been made to describe it.

A close inspection of Table 4 also unravels the enhanced accuracy on the predicted structural parameters when the raw ab initio energies are CBS extrapolated via GUSTE(D,T). In fact, the computed CHIPR values for R_e , D_e , and w_e are within $\approx 0.003 \text{ a}_0$, $\approx 10 \text{ kJ mol}^{-1}$, and $\approx 10 \text{ cm}^{-1}$, respectively, of the experimental data. Note that excellent correlations were also found between such attributes and those predicted from the best CBS protocols utilized here, GUSTE(5,6), as well as the most reliable results from the literature.^{22,56,64}

To assess the quality of the GUSTE(D,T) curves, we compare the deviations of the calculated⁶⁷ vibrational band origins and available experimental and theoretical data in Table 5; see the extended version in the SI. The enhancement in quality by extrapolating to the CBS limit is remarkable; see Table S2. Note that the GUSTE(D,T) and GUSTE(5,6)

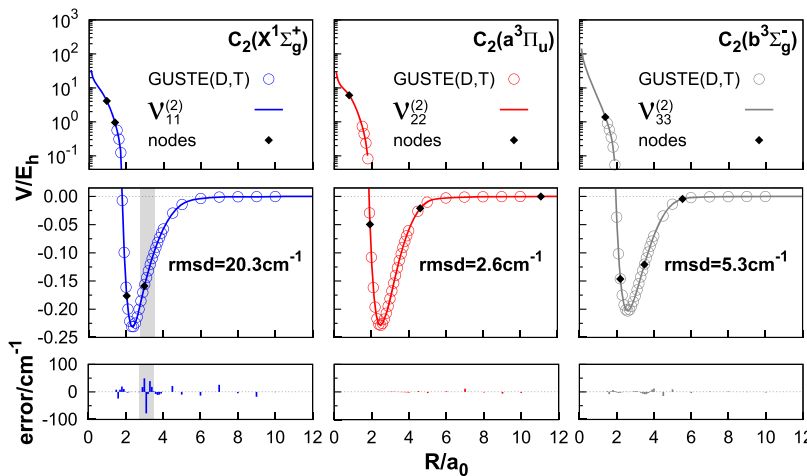


Figure 5. CHIPR potential energy curves for $C_2(X^1\Sigma_g^+)$, $C_2(a^3\Pi_u)$ and $C_2(b^3\Sigma_g^-)$. Open symbols indicate the ab initio GUSTE(D,T) energies, while the lines represent the fitted analytic CHIPR functions of eq 12. Solid diamonds indicate the origins (R_{α}^{ref}) of each primitive basis ϕ_{α} of eq 6. For $C_2(X^1\Sigma_g^+)$, the shaded area highlights the region of larger deviations associated with the presence of an avoided crossing with the next $B^1\Sigma_g^+$ state.

protocols yield virtually the same attributes for C_2 near the equilibrium geometry (Table 4), with the deviations obtained for the latter ($rmsds \approx 40 \text{ cm}^{-1}$) being only 30 cm^{-1} better than the former. This reiterates the high computational demand needed for the accurate determination of C_2 spectroscopy.⁶⁶ As noted elsewhere,^{22,55,56,66} any better agreement with experiment for this interesting molecule requires the inclusion of core/core-valence (CBS extrapolated) correlation,⁵⁶ scalar relativistic corrections,⁶⁴ extrapolation to the N -electron basis set limit, e.g., via the DMBE-scaled external correlation (DMBE-SEC) method,²² and eventually a final (albeit small) touch from the experimental data.⁶⁶ We follow the latter approach using as diagonal elements of the pre-diagonalized potential matrix in eq 11 curves that were modeled from a direct fit to the available spectroscopic data.^{68,69} Specifically, we have followed refs 68 and 69 by determining the parameters of the CHIPR curves via a fine-tuning minimization of

$$\chi^2 = \sum_{j=1}^{N_a} \{W_j^a [V_{ii}^{(2)}(R_j; C_k, c_{\alpha}) - E^{\text{CBS}}(R_j)]^2 + \sum_{j=1}^{N_b} [W_j^b (\tilde{\nu}_j^{\text{calc}} - \tilde{\nu}_j^{\text{exp}})]^2 + [W^c (w_e^{\text{calc}} - w_e^{\text{exp}})]^2 + [W^d (D_e^{\text{calc}} - D_e^{\text{exp}})]^2 + \left[W^e \frac{dV_{ii}^{(2)}(R; C_k, c_{\alpha})}{dR} \right]_{R=R_e^{\text{exp}}}^2 \} \quad (14)$$

where E^{CBS} refers to the GUSTE(D,T) energies, $\tilde{\nu}$ to the transition frequencies, and the last three terms ensure that the final curves reproduce, respectively, the experimental harmonic frequencies, dissociation energies, and equilibrium geometries are given in Table 4; the W 's are the associated least-squares weights. Recall that C_k and c_{α} in eq 14 are the polynomial and contraction basis set coefficients to be optimized. For the spectroscopic data, we have included all observed vibrational band origins reported in ref 62 (see its Figure 1), which, for the $^3\Pi_u$ and $^3\Sigma_g^-$ states, comprise a total of $N_b = 14$ and 7 levels,

respectively. Note that for the $^1\Sigma_g^+$ state, only levels with outer classical turning points below $\approx 2.8 \text{ } a_0$ were added in eq 14, which amounts to $N_b = 6$. This is justified by the fact that there are nonadiabatic effects that we have not rigorously taken into account; all vibrational calculations have been carried out with LEVEL.⁶⁷ All fits utilized $W^a = 0.1$ for ab initio energies, $W^{c,d,e} = 10^2$ for structural parameters (w_e , D_e and R_e), and $W^b = 10^4$ for transition frequencies. The final curves so obtained are compared with the GUSTE(D,T) ones in Figure 6, while Tables 4 and 5 show their attributes; all refined coefficients of eq 12 are given as the SI. Clearly, the fitted potentials reproduce the experimental force fields and vibrational transition frequencies with an rmsd well below spectroscopic accuracy ($\approx 1 \text{ cm}^{-1}$). Moreover, Figure 6 shows that they differ from their purely ab initio curves only in the attractive region of the potential. Despite this and the fact that such potentials are slightly deeper than the GUSTE by approximately the same energy, all $R_{c_{ij}}$ crossing points suffer no significant change relative to the ab initio values. This may support our strategy of replacing the diagonal ab initio curves of eq 11 by realistic curves.⁷⁰ To denote this, we add a subscript “exp” in $V_{\text{exp}}^{(2)}$ to signal their slightly empirical nature. Note that the replacement of the purely ab initio curves by the latter is only performed after calculating and fitting the three-body energies: to signal this, we recall CHIPR-2BD-EXP to the final PES so obtained.

3.3. Three-Body Terms. Once the two-body potentials are obtained, the three-body energy $\epsilon^{(3)}$ is then defined by

$$\epsilon^{(3)}(\mathbf{R}) = E^{\text{CBS}}(\mathbf{R}) - \sum_{i=1}^3 V^{(2)}(R_i) \quad (15)$$

where E^{CBS} is the USTE(D,T) interaction energy (defined with respect to the infinitely separated C atoms) for any geometry of the triatomic and $V^{(2)}$ represents the lowest eigenvalue of eq 11 using the purely ab initio diagonal curves.

Specifically, for an A_3 -type molecule, eq 5 reduces to^{37,38}

$$V_S^{(3)}(\mathbf{R}) = \sum_{i,j,k=0}^L C_{i,j,k} \left(\sum_{g \in G} \mathcal{P}_g^{(i,j,k)} y_1^i y_2^j y_3^k \right) \quad (16)$$

Table 4. Equilibrium Geometries (R_e in a_0), Dissociation Energies (D_e in kJ mol^{-1}), and Harmonic Vibrational Frequencies (w_e in cm^{-1}) of C_2

	method ^a	R_e	D_e	w_e
$\text{C}_2(\text{X}^1\Sigma_g^+)$	CAS/AVDZ	2.394	589.5	1843.2
	MRCI(Q)/AVDZ	2.408	536.8	1800.5
	CAS/AVTZ	2.372	605.8	1839.1
	MRCI(Q)/AVTZ	2.367	583.3	1828.8
	MRCI(Q)/AV6Z	2.355	600.4	1849.1
	GUSTE(5,6)	2.354	608.3	1850.1
	CHIPR ^b	2.349	608.5	1841.6
	CHIPR ^c	2.348	618.6	1855.5
	CBS ^d	2.347	617.1	1860.7
	exp. ^e	2.348	618.6	1855.0
$\text{C}_2(\text{a}^3\Pi_u)$	CAS/AVDZ	2.535	548.8	1602.2
	MRCI(Q)/AVDZ	2.539	540.3	1588.8
	CAS/AVTZ	2.513	559.8	1597.8
	MRCI(Q)/AVTZ	2.499	581.4	1613.9
	MRCI(Q)/AV6Z	2.487	595.4	1630.6
	GUSTE(5,6)	2.486	600.1	1632.5
	CHIPR ^b	2.481	600.8	1628.5
	CHIPR ^c	2.479	610.0	1641.4
	DMBE-SEC ^f	2.483	610.0	1638.3
	exp. ^e	2.479	610.0	1641.3
$\text{C}_2(\text{b}^3\Sigma_g^-)$	CAS/AVDZ	2.638	473.9	1437.7
	MRCI(Q)/AVDZ	2.644	478.8	1428.9
	CAS/AVTZ	2.616	482.9	1436.2
	MRCI(Q)/AVTZ	2.607	516.0	1448.3
	MRCI(Q)/AV6Z	2.596	529.2	1471.9
	GUSTE(5,6)	2.595	533.8	1462.6
	CHIPR ^b	2.593	533.5	1454.8
	CHIPR ^c	2.587	541.6	1470.4
	MRCI(Q)/ACV6Z ^g	2.588		1470.5
	exp. ^e	2.587	541.6	1470.4
$V_{\text{exp}}^{(2)}\text{h}$	CHIPR	2.351	608.7	1819.1
$V_{\text{exp}}^{(2)}\text{i}$	CHIPR	2.349	618.7	1838.4

^aThis work unless stated otherwise. ^bFitted ab initio GUSTE(D, T) energies using the CHIPR functional form of eq 12. ^cExperimentally determined CHIPR potentials via multiproperty fit to experimental data; see the text. ^dRef 56. From the USTE(Q,S) potential energy curve calibrated with MRCI(Q)/ACVXZ energies. ^eRefs 62 and 63. ^fRef 22. ^gRef 64. Includes scalar relativistic effects. ^hLowest state arising from the diagonalization of eq 11. ⁱAs in (h), but using experimentally determined CHIPR curves.

where $C_{ij,k}$ are coefficients and y_p ($p = 1, 2, 3$) contracted basis in eq 6. Following ref 38, all $C_{ij,k}$ terms up to a given L are considered, subject to the constraints: $i + j + k \neq i \neq j \neq k$, $i + j + k \leq L$ and $i \leq j \leq k$, the first being especially chosen to ensure that at least two modes are excited, such as to leave out any two-body energies.^{37,38} In eq 16, the second summation runs over all possible (permutation) elements $g \in G$, where G is a subgroup of the symmetric group.⁷¹ Thus, $\mathcal{P}_g^{(i,j,k)}$ is the corresponding permutation operator that acts on the (exponent) set $\{i(1), j(2), k(3)\}$; the numbers in parenthesis are dummy indices. This will generate the required symmetrized sum of monomials, all invariant with respect to permutations of identical atoms. For completeness, we list in Table 6 all $\mathcal{P}_g^{(i,j,k)}$ operators (in cycle notation⁷¹) and the subgroup structure of S_3 allowed for a given i, j, k set. The above method has some resemblance with the so-called

permutationally invariant polynomial (PIP) approach^{72,73} (particularly, in its monomial symmetrization variant), which, for the case of A_3 -type species, has been applied^{74,75} to O_3 . Despite such obvious similarities, it is on their differences that we focus next. The first and most obvious relates to the fact that rather than representing total energies, in CHIPR only three-body terms are fit with eq 16. Besides warranting by built-in the proper description of all dissociation limits (a long-standing asset of MBE-type theories^{15,52}), such an n -body decomposition of the total energy makes the appearance of formal constraints in eq 16. These are related to the exclusion of two-body contributions as noted above. Thus, as pointed out elsewhere,³⁹ the allowed number of three-body $C_{i,j,k}$ coefficients are $L + 1$ smaller when compared with total energy PIPs.⁷⁴ The second and not less relevant difference relates to the functional form used for the transformed coordinates. While Morse-like variables [$y_p = \exp(-R_p/\lambda)$, where λ is a nonlinear parameter] have been advocated for PIPs,^{72,74,75} the use of contracted basis sets (eq 6) in CHIPR is intended not only to provide a physically correct description in the limit of asymptotically large R_p but also to capture much of the underlying chemistry (see below). As noted,³⁷ the chosen primitives of eqs 7 and 8 (and, particularly, their combination) provide a consistent set that may suitably mimic the proper inverse-power dependence on the atom–diatom distance at long-range while having a convenient quasi-localized Gaussian-like form expected for n -body terms.

The calibration of eq 16 has been done by minimizing the sum of squared residuals

$$\chi^2 = \sum_{I=1}^N \{W_I[V_I^{(3)}(\mathbf{R}; C_{i,j,k}, c_\alpha) - \epsilon_I^{(3)}(\mathbf{R})]\}^2 \quad (17)$$

where I runs over the $N = 5999$ calculated triatomic GUSTE(D, T) grid points, and all other quantities have the meaning given above.

The first step therefore consists of setting the contracted basis sets in eq 6. Since the title system is composed of three identical carbon atoms, all transformed coordinates must reflect the appropriate symmetry constraint: $y_1 \equiv y_2 \equiv y_3 \equiv y$. Following the usual procedure,³⁷ a 1D ab initio cut along the line of D_{3h} symmetry has been selected and the parameters of eqs 6–9 determined from a fit to the resulting three-body energies; see Figure 7. Note that, similarly to the two-body case, both primitive basis in eqs 7 and 8 were utilized here, with the latter equation appearing only once as the last term in eq 6. As shown in Figure 7, a contraction containing 22 parameters (hereinafter denoted as b22) is required to obtain an accurate description of the data over the full range of fitted distances (correspondingly, a b10 basis is sufficient for the two-body curves in Figure 5). Also shown by the solid diamonds are the distributed origins R_α^{ref} of each primitive basis ϕ_α in eq 6; the corresponding nonlinear parameters γ_α , ζ , and R^{ref} (eqs 6–9) have been optimized by trial-and-error and kept fixed in all subsequent steps.

Having b22, the determination of the polynomial coefficients in eq 16 has been as follows. First, all contraction coefficients assumed the values previously optimized and the $C_{ij,k}$ coefficients of the input row-vector set to a unit value. The solution so obtained was then utilized as the initial guess for subsequent optimizations with all parameters (including c_α) varying freely. The final optimized contracted basis is also shown in Figure 7. Regarding the weights, all calculated points

Table 5. Deviations (Observed-Calculated) of Vibrational Bands, in cm^{-1} , for C_2 As Calculated with CBS Energies; See Table S2 for an Extended Version

v	$\text{C}_2(\text{X}^1\Sigma_g^+)^a$				$\text{C}_2(\text{a}^3\Pi_u)^a$				$\text{C}_2(\text{b}^3\Sigma_g^-)^a$			
	CBS ^b	CBS ^c	CHIPR ^d	CHIPR ^e	CBS ^b	CBS ^c	CHIPR ^d	CHIPR ^e	CBS ^b	CBS ^c	CHIPR ^d	CHIPR ^e
1	17.9	11.2	17.6	-0.07	13.6	9.0	13.6	-0.03	11.9	8.4	12.2	-0.02
2	36.4	22.7	35.9	0.01	27.1	17.9	27.2	-0.02	23.6	16.7	24.1	-0.01
3	55.4	34.5	54.7	0.05	40.5	26.6	40.6	0.00	34.9	24.7	35.8	0.02
4	74.9	46.2	74.1	0.01	53.8	35.1	54.0	0.01	46.1	32.6	47.2	0.04
5	95.1	58.3	94.4	-0.06	67.0	43.6	67.3	0.02	57.1	40.3	58.3	0.05
6	116.1	72.6	115.7	0.02	80.1	51.8	80.5	0.02	68.0	47.8	69.1	0.05
7					93.1	60.0	93.6	0.01	78.8	55.2	79.7	0.03
8					106.1	68.0	106.7	-0.01				
9					119.0	75.9	119.6	-0.02				
rmsd	74.0	45.9	73.5	0.04	74.8	48.2	75.2	0.02	50.9	35.8	51.8	0.03

^aExperimental band origins taken from ref 62. All energies are relative to the appropriate $v = 0$ vibrational level. ^bThis work. From spline fit to ab initio GUSTE(D,T) energies. ^cThis work. From spline fit to ab initio GUSTE(5,6) energies. ^dThis work. Fitted ab initio GUSTE(D,T) energies using the CHIPR functional form of eq 12. ^eThis work. Experimentally determined CHIPR potentials via multiproperty fit to experimental data; see the text.

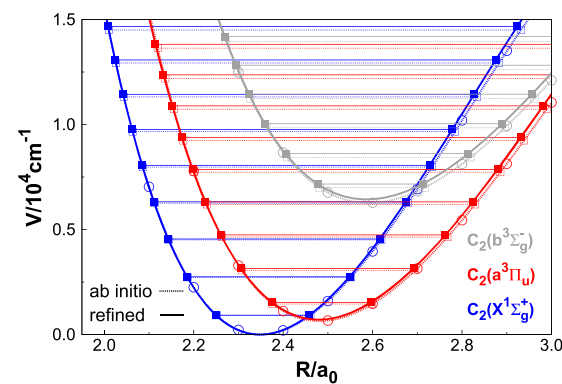


Figure 6. Vibrational levels and classical turning points (open and filled squares) calculated with the purely ab initio and experimentally determined CHIPR potentials. Open circles indicate GUSTE(D,T) energies. The zero of energy is set relative to the corresponding ground-state C_2 curves.

carried a unit value except the ones with $2.2 \leq R_{1,2}/a_0 \leq 3.0$ at $\angle \text{CCC}/\text{deg} = 60, 70, 100, 110, 120, 170, 180$, which carried a weight of 2. Adding to this, all points with $E^{\text{CBS}} \gtrsim 1250 \text{ kJ mol}^{-1}$ above the global minimum carried a 0.5 weight. To avoid unphysical holes at high energy regions (close to the united-atom limit), we have then multiplied the three-body term in eq 16 by³⁷

$$\mathcal{D}(\mathbf{R}) = \left[\prod_{i=1}^3 h(R_i) \right]^\xi \quad (18)$$

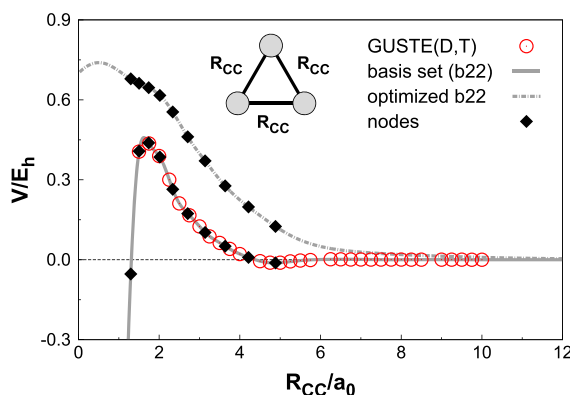


Figure 7. C–C contracted basis set from a fit to GUSTE(D,T) three-body energies (open red circles) for equilateral triangular geometries of triplet C_3 . Solid diamonds indicate the origins (R_α^{ref}) of each primitive basis ϕ_α in eq 6.

where $h(R_i) = \frac{1}{2} \{1 + \tanh[\kappa(R_i - R_0)]\}$. This warrants that the three-body term vanishes for large negative displacements from a chosen reference $R_0 = 0.5 a_0$ while becoming unit for large positive ones; $\kappa = 100 a_0^{-1}$ and $\xi = 10$. Indeed, the three-body term is expected to contribute negligibly in relative terms at such regions of the PES.³⁷

With the CHIPR method, we have been able to fit with eq 16 all 5999 ab initio points with an rmsd of 2.7 kJ mol^{-1} ; the procedure involved 683 linear parameters in the polynomial expansion and a symmetrized sum of monomials up to the

Table 6. Operators $\mathcal{P}_g^{(i,j,k)}$ and Subgroup Structure of the Symmetry Group S_3 for a Given Exponent Set $\{i(1), j(2), k(3)\}^a$

case	$\mathcal{P}_g^{(i,j,k)}$	subgroup G	subgroup name
$i = j = k$	($)$	$\{()\}$	trivial group
$i = j \neq k$	$(), (1,3), (2,3)$	$\{(), (1,3)\}, \{(), (2,3)\}$	cyclic group Z_2
$i \neq j = k$	$(), (1,2), (1,3)$	$\{(), (1,2)\}, \{(), (1,3)\}$	cyclic group Z_2
$k = i \neq j$	$(), (1,2), (2,3)$	$\{(), (1,2)\}, \{(), (2,3)\}$	cyclic group Z_2
$i \neq j \neq k$	$(), (1,2), (1,3), (2,3), (1,2,3), (1,3,2)$	$\{(), (1,2), (1,3), (2,3), (1,2,3), (1,3,2)\}$	symmetric group S_3

^aNumbers given in parentheses are dummy values. ^bAll permutations are in cyclic notation.⁷¹ ($)$ is the identity operator, and (x,y) and (x,y,z) are two- and three-cycle permutations. For example, $(1,2)$ permutes i (1) and j (2), $(2,3)$ permutes j (2) and k (3), and $(1,2,3)$ sends i (1) to j (2), j (2) to k (3), and k (3) back to i (1).

power 26. Table 7 displays the stratified rmsd. Figure 8 shows the distribution of errors in all fitted data. Clearly, a normal

Table 7. Stratified Root-Mean-Square Deviations (in kJ mol^{-1}) of the Final PES

energy ^a	N ^b	max. dev. ^c	rmsd	N _{>rmsd} ^d
50	187	3.9	1.0	50
100	248	3.9	0.9	67
150	393	8.0	1.4	75
200	538	15.3	1.9	108
300	951	15.3	2.3	205
400	1319	17.6	2.5	265
600	2124	23.4	2.8	420
800	4121	23.4	2.5	735
1000	5316	23.4	2.6	925
2000	5813	28.4	2.7	951
3000	5980	28.4	2.7	1001
4000	5997	28.4	2.7	1007
7000	5999	28.4	2.7	1003

^aThe units of energy are kJ mol^{-1} . Energy strata defined relative to the D_{3h} absolute minimum of C_3 with the energy of -0.4774 E_h .

^bNumber of calculated points up to the indicated energy range.

^cMaximum deviation up to indicated energy range. ^dNumber of calculated points with an energy deviation larger than the rmsd.

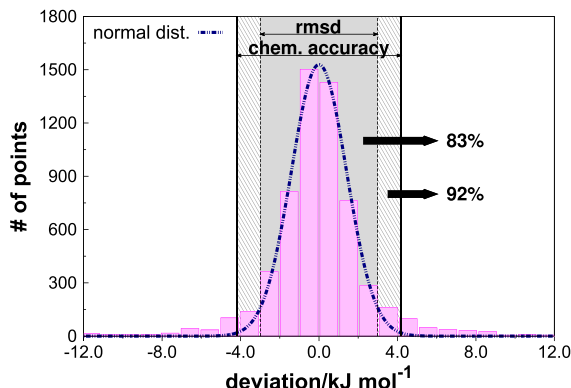


Figure 8. Distribution of deviations between calculated and fitted ab initio points. The curve indicates a normal distribution adjusted to the data. The shaded area highlights the fraction of the population falling within chemical accuracy and rmsd error margins, with their corresponding percentages also given.

distribution pattern is observed, with 83% of the errors falling within the rmsd. Remarkably, 92% of the data shows chemical accuracy; see the SI for least-squares parameters, and Figure S1 for the performance of the final CHIPR form.

4. FEATURES OF THE PES

All major features of the CHIPR PES are depicted in Figures 9–13 while the properties of its stationary points are in Table 8; also included are results from the literature.^{19,25,27,29,30,32–34} Since both CHIPR and CHIPR-2BD-EXP forms have similar attributes, we focus on the former but address, where appropriate, their most marked differences.

A notable feature on the triplet C_3 PES relates to the fact that its global minimum attains an equilateral triangular conformation [$\text{Min}(D_{3h})$] with a characteristic bond length of 2.590 \AA . As Table 8 shows, the corresponding value predicted from the CHIPR-2BD-EXP PES differs by $<0.01 \text{ \AA}$. As noted elsewhere,⁷⁰ the overall changes are minor when introducing

experimental diatomic curves into the potential (recall that C_2 curves are already at the CBS level), with the fundamental frequencies emerging as the most sensitive property. This is a virtue of CHIPR due to employing a full MBE.^{37–39} The above is particularly true for $\text{Min}(D_{3h})$, where the contributions of the two-body terms in eq 4 are maximized. Indeed, its a'_1 and e' frequencies show an increase of about $30\text{--}40 \text{ cm}^{-1}$ when compared with the ones predicted from the CHIPR PES; see Table 8. Although it is difficult to judge which are more realistic [since no experimental data is available for $\text{C}_3(^3\text{A}'_2)$], it will be shown later that, for the case of the linear isomer [$\text{Min}(D_{\infty h})$], the accuracy of all its attributes are slightly enhanced whenever direct-fit curves are set in eq 11. This assessment is in general agreement with the recently proposed DMBE-STE approach by Varandas and Galvão⁷⁰ who advocated the use of simple (multiplicative) scaling factors in the various (fitted) n -body terms to bring MBE/DMBE forms and their predicted properties into consistency with experiment.

As shown in Figures 10–13, $\text{Min}(D_{\infty h})$ arises as a local minimum on the PES with a characteristic bond length of $R_1 = R_2 = R_3/2 = 2.467$ and 2.466 \AA predicted from the CHIPR and CHIPR-2BD-EXP forms, respectively. These values are in excellent agreement with the experimental r_e value reported by Tokaryk and Civis¹⁸ of 2.466 \AA . $\text{Min}(D_{\infty h})$ thus lies about $126.9 \text{ kJ mol}^{-1}$ above $\text{Min}(D_{3h})$, a value that is quite close to $125.4 \text{ kJ mol}^{-1}$ from GUSTE(5,6). This is to be compared with the energy difference of $136.1 \text{ kJ mol}^{-1}$ predicted from CHIPR-2BD-EXP. Indeed, as noted in ref 70, the present “scaling” of the two-body energy terms naturally corrects for core–core/core–valence correlation, truncation of the N -electron expansion, non-adiabaticity, and relativistic effects, thence explaining to a large extent the observed discrepancies in the relative energies;⁷⁰ see comparison in Figure 13. The $\text{Min}(D_{\infty h})$ ’s fundamentals calculated⁷⁷ with the CHIPR (CHIPR-2BD-EXP) PES deviate by 2.5 (8.9) and -54.5 (-37.9) cm^{-1} relative to the experimental^{26,27} ν_1 and ν_3 band origins, respectively. The corresponding difference in ν_2 (from the harmonic RT case¹⁸) is 134.2 (141.3) cm^{-1} . Although the CHIPR form accurately mimics the region nearby $\text{C}_3(\tilde{\alpha}^3\Pi_u)$ (Figure 9b), the present adiabatic nuclear calculations (see below) lack the proper (electronic + spin + vibrational + rotational) angular momentum couplings required to correctly describe an RT interaction.^{16,17,78,79} Thus, small discrepancies (particularly on bending states) should a priori be expected between the observed and calculated transition frequencies. A notable aspect on the underlying PES, first remarked by Fueno and Taniguchi,³² is that, at the CAS level, $\text{Min}(D_{\infty h})$ appears as a first-order saddle point whose imaginary frequency (2541.4 cm^{-1}) corresponds to the antisymmetric stretching vibration (ω_3). In fact, our CAS/AVTZ calculations confirm the appearance of a true (asymmetric) $^3\Pi_u$ minimum by following this mode that lies $\approx 1 \text{ kJ mol}^{-1}$ lower in energy than the $^3\Pi_u$ structure (Table 8). A similar double-minimum potential along ω_3 has also been reported by Izuha and Yamanouchi⁸⁰ for the $\tilde{\alpha}^1\Pi_u$ state. Different from this latter case,^{32,80} the addition of dc in MRCl calculations reverses the stability of the above forms and make $^3\Pi_u$ a local minimum on the PES. Moreover, as noted by Fueno and Taniguchi, it turns out that the use of more accurate methods, such as the GUSTE(D,T) employed here, stabilize even further the $D_{\infty h}$ isomer. We failed to locate any $C_{\infty v}$ stationary point on the triplet PES at the MRCl level.

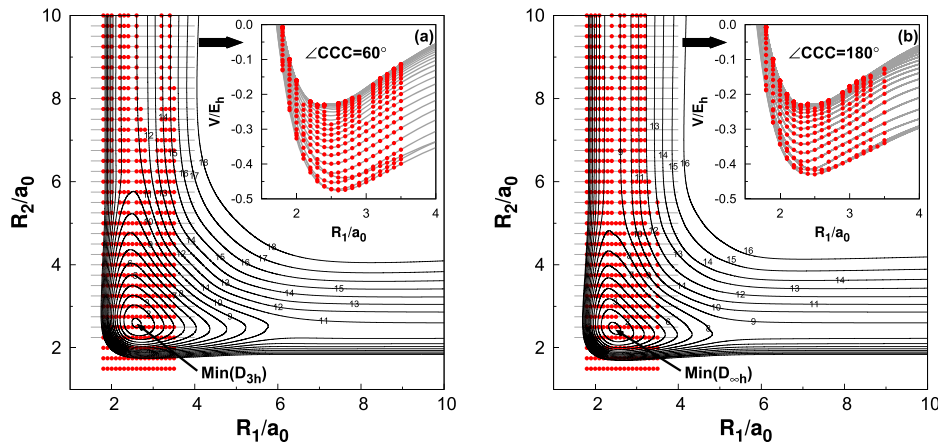


Figure 9. Sample CHIPR PES contour plots for the C–C–C bond stretching for valence angles of (a). $\angle \text{CCC} = 60^\circ$ and (b). $\angle \text{CCC} = 180^\circ$. Contours equally spaced by 0.025 E_h , starting at $-0.5 E_h$. Solid dots indicate ab initio GUSTE(D, T) points; see also Figure S1 to assess all angular cuts and data set. The zero of energy is set relative to the infinitely separated C atoms.

Table 8. Structural parameters (R_i in a_0 , θ in degrees), harmonic (w_i), and fundamental (ν_i) frequencies (in cm^{-1}) of the stationary points on the ground-state triplet PESs of C_3^{α}

structure	method ^b	R_1	R_2	θ	ΔE^b	$w_1 (\nu_1)$	$w_2 (\nu_2)$	$w_3 (\nu_3)$
$\text{Min}(D_{3h})$	CAS/AVTZ	2.629	2.629	60.0	0.0	1508.3	1064.2	
	MRCI(Q)/AVTZ	2.614	2.614	60.0	0.0	1539.4	1102.5	
	GUSTE(5,6) ^c				0.0			
	MP4/6-31G* ^d	2.543	2.543	60.0		1774.0	1091.0	
	MRCI/6-311+G* ^e	2.632	2.632	60.0	0.0			
	CCSD(T)/6-311+G(3df,2p) ^f	2.587	2.587	60.0		1618.0	1155.0	
	B3LYP/6-311+G* ^g	2.588	2.588	60.0	0.0	1616.0	1157.0	
	CHIPR	2.590	2.590	60.0	0.0	1511.2	1049.9	
						(1488.3)	(1064.0)	
	CHIPR-2BD-EXP	2.580	2.580	60.0	0.0	1549.9	1092.5	
						(1522.7)	(1095.9)	
$\text{TS}(C_{2v})$	CAS/AVTZ	2.510	2.622	104.7	239.0	1265.0	994.3i	1557.3
	MRCI(Q)/AVTZ	2.488	2.613	106.5	268.0			
	GUSTE(5,6) ^c				280.1			
	MRCI/6-311+G* ^e	2.523	2.621	103.2	272.1			
	CHIPR	2.528	2.528	107.4	278.7	1336.2	1013.8i	676.1
	CHIPR-2BD-EXP	2.520	2.520	107.5	290.8	1356.6	1024.1i	743.7
$\text{Min}(D_{\infty h})$	CAS/AVTZ	2.489	2.489	180.0	86.3	1144.8	169.5/370.0 ^h	2541.4i
	CAS/AVTZ	2.440	2.532	180.0	85.3	1139.5	193.2/368.1 ^h	1428.6
	MRCI(Q)/AVTZ	2.482	2.482	180.0	114.9			
	GUSTE(5,6) ^c				125.4			
	MRCI/6-311+G* ^e	2.489	2.489	180.0	175.6			
	B3LYP/6-311+G* ^g	2.446	2.446	180.0				
	MRCI/DZP ⁱ	2.477	2.477	180.0		1209.0	415.0/467.0 ^h	1344.0
	CHIPR	2.467	2.467	180.0	126.9	1147.0	553.7	1344.2
						(1159.0)	(491.4)	(1395.0)
	CHIPR-2BD-EXP	2.466	2.466	180.0	136.1	1145.3	554.5	1339.5
$\text{SP}_2(C_{2v})$	exp.	2.466 ^j	2.466	180.0		(1165.4)	(498.5)	(1411.6)
	GUSTE(5,6) ^c				649.6	1156.5 ^k	357.2 ± 13 ^l	1449.5 ^k
	CHIPR	6.595	6.595	20.7	648.3	93.0i	1555.6	73.2i

^aRelative energies (ΔE) are in kJ mol^{-1} and given with respect to the D_{3h} global minimum. ^bThis work unless stated otherwise. ^cGUSTE(5,6) single-point energies calculated at CHIPR PES stationary points. ^dRef 30. ^eRef 32. ^fRef 33. ^gRef 34. ^hThe two calculated partners of the expected double-degenerate frequency are separated by the dash. ⁱRef 29. ^j r_e value obtained from $B_e = 0.41261 \text{ cm}^{-1}$ reported in ref 18. ^kRefs 26 and 27. ^lEnergy difference between $(0,0,0)^3\Pi_u$ and $(0,1,0)^3\Sigma_g^-$ vibronic levels predicted from the harmonic Renner–Teller model of ref 19.

The conversion of $\text{Min}(D_{3h})$ into the $\text{Min}(D_{\infty h})$ minima occurs via $\text{TS}(C_{2v})$ transition state; this is clearly visible from the plots in Figures 10 and 11, which depict contours for a C atom moving around C_2 and the corresponding T-shaped

(C_{2v}) insertion. Indeed, $\text{TS}(C_{2v})$ is located at $R_1 = R_2 = 2.528$ and $R_3 = 4.073 a_0$ with an imaginary frequency of $1013.8i \text{ cm}^{-1}$ along the bending (w_2) mode. Such attributes deviate by $\approx 0.01 a_0$ and $\approx 10 \text{ cm}^{-1}$ from the values predicted with CHIPR-2BD-

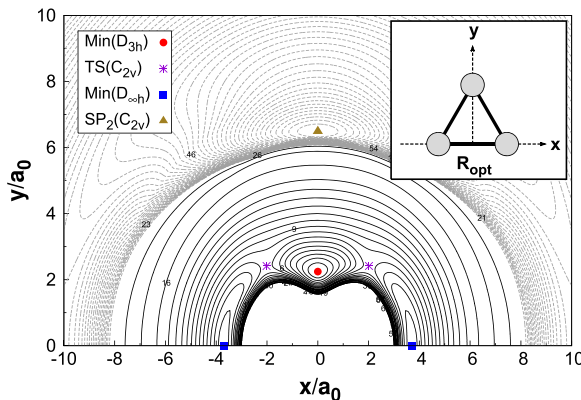


Figure 10. CHIPR contour plot for the C atom moving around a partially relaxed C_2 diatom ($2.2 \leq R/a_0 \leq 2.6$), which lies along the x -axis with the center of the bond fixed at the origin. Black solid and gray dashed lines equally spaced by 0.015 and 0.00001 E_h , starting at -0.5 and $-0.2326 E_h$. The zero of energy is set relative to the infinitely separated C atoms. See also the text.

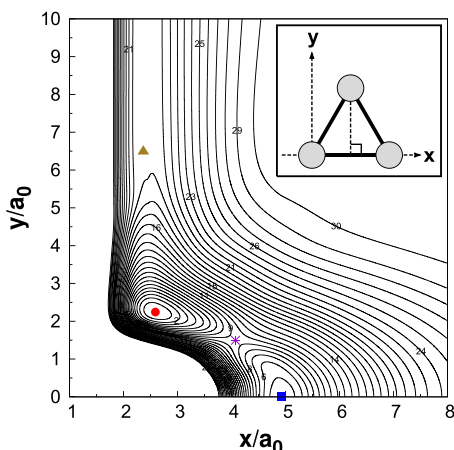


Figure 11. CHIPR contour plot for C_{2v} insertion of the C atom into the C_2 fragment. Contours equally spaced by $0.02 E_h$, starting at $-0.5 E_h$. The zero of energy is set relative to the infinitely separated C atoms. Key for stationary points as in Figure 10.

EXP. The classical barrier height estimated from the present CHIPR PES is $278.7 \text{ kJ mol}^{-1}$ relative to $\text{Min}(D_{3h})$, in excellent agreement with the GUSTE(5,6) estimate of $280.1 \text{ kJ mol}^{-1}$. As seen in Table 8, the isomerization barrier in CHIPR-2BD-EXP is $290.8 \text{ kJ mol}^{-1}$. Suffice it to say that Fueno and Taniguchi³² predicted at the MRCI/6-311+G* level a similar TS but with C_s symmetry; the characteristic bond lengths so found are $R_1 = 2.523$, $R_2 = 2.621$, and $R_3 = 4.032 a_0$. As claimed by the authors, such a structure arises due to the presence of a conical intersection between the first two $^3A'$ states of C_3 at C_{2v} geometries. Our present MRCI calculation supports such a feature (Figure 14), but no evidence so far of an unsymmetrical TS was found. This is a subtle issue that requires further investigation. As noted elsewhere,³⁷ one cannot expect the present single-sheeted formalism to describe per se intrinsic nonanalyticities associated with conical intersections.

As seen from Figure 10, $\text{Min}(D_{3h})$ and $\text{TS}(C_{2v})$ are connected by another saddle point of index 2, $\text{SP}_2(C_{2v})$, with characteristic bond lengths of $R_1 = R_2 = 6.595$ and $R_3 = 2.366 a_0$, which lies about $648.3 \text{ kJ mol}^{-1}$ above $\text{Min}(D_{3h})$. Of course, for the above reason, we cannot discriminate it from an

eventual conical intersection at a long-range. Note that the dissociation of the D_{3h} global minimum into $C_2 + C$ fragments is estimated to be as endothermic as 644.8 and $660.1 \text{ kJ mol}^{-1}$ from CHIPR and CHIPR-2BD-EXP, respectively. The corresponding dissociations to infinitely separated C atoms are 1253.5 and $1278.8 \text{ kJ mol}^{-1}$.

Figure 12 shows a relaxed triangular plot in hyperspherical coordinates⁷⁶ as obtained from the CHIPR PES and depicts in

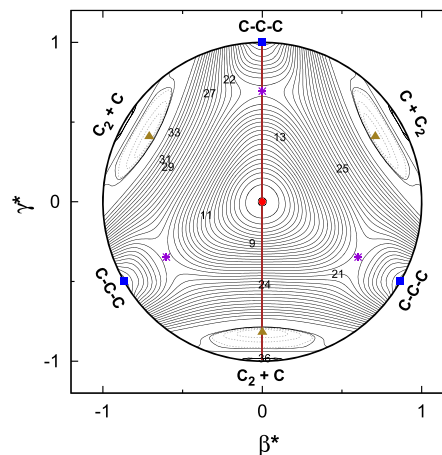


Figure 12. Relaxed triangular plot in hyperspherical coordinates⁷⁶ of the CHIPR PES. Black solid and gray dashed lines are equally spaced by $0.005 E_h$ and $0.00015 E_h$, starting at -0.5 and $-0.23155 E_h$. The line across C_{2v} geometries is plotted in Figure 13 as a 1D cut. The zero of energy is set relative to the infinitely separated C atoms. Key for stationary points as in Figure 10.

a global way all of the stationary structures discussed above. For clarity, we have also plotted in Figure 13 the

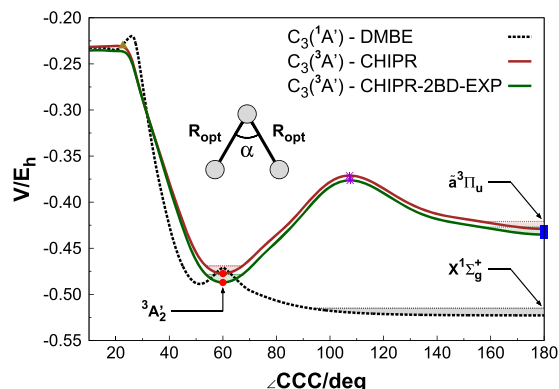


Figure 13. Optimized bending potentials for $C_3(^3A')$ obtained from the CHIPR and CHIPR-2BD-EXP PESs. Also shown for comparison is the corresponding curve for ground-state $C_3(^1A')$ calculated with the DMBE PES of ref 14. Filled areas highlight the region of the configuration space spanned by the zero-point energy (ZPE) levels. The zero of energy is set relative to the infinitely separated C atoms. Key for stationary points as in Figure 10.

corresponding 1D cuts across C_{2v} geometries (highlighted by a solid line in Figure 12) calculated with all C_3 PESs considered here. Accordingly, the global CHIPR analytic forms describe accurately both valence and long-range features of the potentials, including the correct behavior at the $C_2 + C$ asymptote. Moreover, they warrant by built-in construction the proper permutation invariance of like channels, which is no

doubt achieved by the use of appropriate $\mathcal{P}_g^{(i,j,k)}$ operators in eq 16.

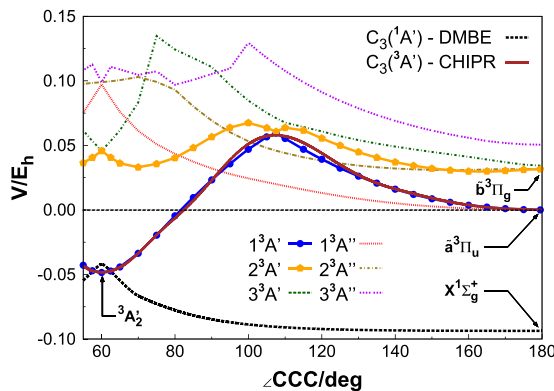


Figure 14. Optimized bending potential for $C_3(^3A')$ obtained from the CHIPR PES. Color solid dots and dashed/dotted curves indicate ab initio GUSTE(D,T) energies calculated using ${}^3(A'$ or A'') states in the CAS/MRCI wave functions. Also shown for comparison is the corresponding curve for ground-state $C_3(^1A')$ obtained with the DMBE PES of ref 14. The zero of energy is set relative to the $C_3(\tilde{a}^3\Pi_u)$ state.

5. SPECTROSCOPIC CALCULATIONS

To assess the quality of the final PES, we have performed bound-state calculations in $C_3(^3A'_2)$ and $C_3(\tilde{a}^3\Pi_u)$ using the multidimensional discrete variable representation (DVR) method as implemented in the DVR3D software suite.⁷⁷ Briefly, our approach employs the general (radial) effective

Table 9. Calculated $J = 0$ Band Origins (in cm^{-1}) of Triplet Cyclic C_3 [Min(D_{3h})] Relative to the $(0,0^0)$ Ground-Vibronic State^a

(v_1, v_2')	$(\Gamma_{\text{el}} \otimes \Gamma_{\text{vib}})^b$	CHIPR	CHIPR-2BD-EXP
(0,1 ¹)	E'	1064.0	1095.9
(1,0 ⁰)	A'_2	1488.3	1522.7
(0,2 ²)	E'	2129.4	2191.7
(0,2 ⁰)	A'_2	2163.3	2222.6
(1,1 ¹)	E'	2540.3	2604.9
(2,0 ⁰)	A'_2	2974.0	3043.0
(0,3 ³)	A'_2	3194.5	3286.2
(0,3 ³)	A'_1	3197.3	3288.4
(0,3 ¹)	E'	3244.3	3331.4
(1,2 ²)	E'	3592.7	3687.2
(1,2 ⁰)	A'_2	3622.9	3715.5
(2,1 ¹)	E'	4008.9	4107.4
(0,4 ⁴)	E'	4261.5	4381.3
(0,4 ²)	E'	4312.4	4427.4
(0,4 ⁰)	A'_2	4332.0	4445.3
(3,0 ⁰)	A'_2	4454.0	4557.7
(1,3 ³)	A'_2	4641.5	4765.5
(1,3 ³)	A'_1	4644.5	4768.5
(1,3 ¹)	E'	4684.1	4805.2
(2,2 ²)	E'	5042.8	5170.9
(2,2 ⁰)	A'_2	5069.1	5196.0

^aZPE levels are 1821.8 and 1876.0 cm^{-1} for CHIPR and CHIPR-2BD-EXP PESs, respectively. ^bVibronic symmetry species, where $\Gamma_{\text{el}} \equiv A'_2$.

Table 10. Calculated $J \leq 3$ Band Origins (in cm^{-1}) of Triplet Linear C_3 [Min($D_{\infty h}$)] Relative to the $(0,0^0,0)$ Ground-Vibronic State^a

(v_1, v_2', v_3)	$(\Gamma_{\text{el}} \otimes \Gamma_{\text{vib}})^b$	CHIPR	CHIPR-2BD-EXP
(0,1 ¹ ,0)	$\sum_g^+ + \sum_g^- + \Delta_g$	491.4	498.5
(0,2 ⁰ ,0)	Π_u	926.2	941.4
(0,2 ² ,0)	$\Pi_u + \Phi_u$	956.2	971.1
(1,0 ⁰ ,0)	Π_u	1159.0	1165.4
(0,3 ¹ ,0)	$\sum_g^+ + \sum_g^- + \Delta_g$	1337.8	1361.9
(0,3 ³ ,0)	$\Delta_u + \Gamma_u$	1394.6	1418.0
(0,0 ⁰ ,1)	Π_g	1395.0	1411.6
(1,1 ¹ ,0)	$\sum_g^+ + \sum_g^- + \Delta_g$	1653.4	1666.9
(0,4 ⁰ ,0)	Π_u	1701.1	1734.7
(0,4 ² ,0)	$\Pi_u + \Phi_u$	1727.9	1761.3
(0,1 ¹ ,1)	$\sum_u^+ + \sum_u^- + \Delta_u$	1866.6	1890.7
(0,5 ¹ ,0)	$\sum_g^+ + \sum_g^- + \Delta_g$	2052.5	2095.6
(1,2 ⁰ ,0)	Π_u	2093.5	2114.9
(0,5 ³ ,0)	$\Delta_u + \Gamma_u$	2100.6	2143.6
(1,2 ² ,0)	$\Pi_u + \Phi_u$	2122.8	2144.1
(0,2 ⁰ ,1)	Π_g	2283.4	2316.2
(0,2 ² ,1)	$\Pi_g + \Phi_g$	2312.3	2344.8
(2,0 ⁰ ,0)	Π_u	2315.9	2329.0
(0,6 ⁰ ,0)	Π_u	2376.1	2427.9
(0,6 ² ,0)	$\Pi_u + \Phi_u$	2397.7	2449.6
(1,3 ¹ ,0)	$\sum_g^+ + \sum_g^- + \Delta_g$	2512.8	2542.9
(1,0 ⁰ ,1)	Π_g	2539.2	2563.3
(1,3 ³ ,0)	$\Delta_u + \Gamma_u$	2567.9	2597.6
(0,3 ¹ ,1)	$\sum_u^+ + \sum_u^- + \Delta_u$	2678.1	2720.2
(0,3 ³ ,1)	$\Delta_g + \Gamma_g$	2732.6	2768.7
(2,1 ¹ ,0)	$\sum_g^+ + \sum_g^- + \Delta_g$	2812.8	2833.2
(0,0 ⁰ ,2)	Π_u	2827.4	2860.8
(1,4 ⁰ ,0)	Π_u	2886.6	2926.0
(1,4 ² ,0)	$\Pi_u + \Phi_u$	2912.5	2951.7
(1,1 ¹ ,1)	$\sum_u^+ + \sum_u^- + \Delta_u$	3013.0	3044.8
(1,0 ⁰ ,3)	Π_g	5383.0	5441.0

^aZPE levels are 1785.6 and 1801.8 cm^{-1} for CHIPR and CHIPR-2BD-EXP PESSs, respectively. ^bVibronic symmetry species, where $\Gamma_{\text{el}} \equiv \Pi_u$.

Hamiltonian of Sutcliffe and Tennyson⁸¹ in Jacobi coordinates. In setting the so-called finite basis representation (FBR),⁷⁷ Morse oscillator-like functions were utilized as a radial basis and Legendre polynomials for the included angle; their parameters are gathered in Table S11. With the above set of weighted orthogonal polynomials and their associated Gaussian quadratures, the FBR-to-DVR transformation ($\mathbf{H}^{\text{DVR}} = \mathbf{T}^\dagger \mathbf{K}^{\text{FBR}} \mathbf{T} + \mathbf{V}^{\text{DVR}}$) is accomplished using the so-called quadrature approximation,⁷⁷ with the corresponding kinetic energy integrals evaluated analytically prior to the transformation process. Final solutions are then obtained from a series of diagonalizations and truncations of the transformed Hamiltonian (\mathbf{H}^{DVR}); the reader is addressed to refs 77 and 14 for further details.

Tables 9 and 10 gather the first few rovibrational band origins so obtained, while their corresponding spectroscopic attributes are in Table 11. These were obtained from a fit to the anharmonic spectrum⁵³

$$G_{[v]} = \sum_i \tilde{w}_i \left(v_i + \frac{d_i}{2} \right) + \sum_i \sum_j x_{ij} \left(v_i + \frac{d_i}{2} \right) \left(v_j + \frac{d_j}{2} \right) + g_{22} l^2 \quad (19)$$

Table 11. Summary of Spectroscopic Parameters (in cm^{-1}) of the Triplet Cyclic [Min(D_{3h})] and Linear [Min($D_{\infty h}$)] C_3 Calculated from the CHIPR and CHIPR-2BD-EXP PESs^a

parameter	$C_3(^3A'_2)$		$C_3(\tilde{\alpha}^3\Pi_u)$		
	CHIPR	CHIPR-2BD-EXP	CHIPR	CHIPR-2BD-EXP	exp.
ZPE	1821.8	1876.0	1785.6	1801.8	
T_e^b	9953.1	7831.4	20564.7	19210.1	
T_0^b	10069.8	8002.3	20645.2	19306.8	17090.0 ± 210^c
A_e	0.74812	0.75357			
B_e	1.49624	1.50714	0.41208	0.41234	0.41261 ^d
A_0	0.73904	0.74457			
B_0	1.48424	1.49521	0.41179	0.41206	0.41696 ^e
r_e	2.58953	2.58015	2.46718	2.46641	2.46560 ^d
r_0	2.60268	2.59306	2.46805	2.46722	2.45270 ^e
\tilde{w}_1	1509.0	1546.3	1164.4	1167.0	
\tilde{w}_2	1071.9	1107.6	535.5	542.4	542.3 ± 13^f
\tilde{w}_3			1381.4	1394.2	
x_{11}	-2.5	-2.8	-1.2	-0.3	
x_{22}	3.3	2.2	-17.0	-16.7	
x_{33}			19.2	20.2	
x_{12}	-15.0	-16.1	4.8	5.0	
x_{13}			-14.6	-12.1	
x_{23}			-17.7	-17.6	
g_{22}	-5.0	-4.6	6.4	6.3	

^aBond lengths are in a_0 . ^bRelative to the ground-state $C_3(\tilde{\chi}^1\Sigma_g^+)$. Energies obtained from the corresponding DMBE PES of ref 14. ^cRef 23. ^dRef 18. ^eRef 25. ^fRef 19.

where $G_{[v]}$ denotes the (ro) vibrational level under consideration (in cm^{-1} relative to the bottom of the well); v_1 , v_2 , and v_3 are vibrational quantum numbers (v_1 and v_3 for symmetric and antisymmetric stretching, v_2 for bending), with l in v_2^l being the vibrational angular momentum quantum number ($l = v_2, v_2 - 2, \dots, 0$ or 1). In eq 19, \tilde{w}_i are the harmonic frequencies, x_{ij} and g_{22} are anharmonicity constants, and d_i the associated degeneracy (1 or 2). Note that, for Min($D_{\infty h}$), an extra term $B_0[J(J + 1) - l^2]$ has been added in eq 19 to account for the rotational and vibrational angular momentum effects on states with $J > 0$; B_0 is the rotational constant (that includes zero-point vibrational corrections), and J the total angular momentum quantum number. All levels in Tables 9 and 10 have been fitted by eq 19 with an rmsd of 4–5 cm^{-1} (1%).

Some remarks are due on the definition of the vibronic symmetry species in $C_3(\tilde{\alpha}^3\Pi_u)$. Since our calculations neglect the interaction of the electronic ($\Lambda\hbar$) and vibrational ($I\hbar$) angular momenta, we assume that all levels with vibronic angular momentum quantum number⁵³ $K = |\pm\Lambda \pm l|$ coincide for a given l ; degeneracies (as indicated by the sum of species) in Table 10 correspond to $\Sigma, \Pi, \Delta, \dots$ states for $K = 0, 1, 2, \dots$. If the RT effect⁵³ were considered, one might expect the resolution of all K states (P if spin-orbit effects are included⁵³), with their energies being split accordingly.^{19,53,78}

We start the present discussion by assessing the calculated properties of $C_3(\tilde{\alpha}^3\Pi_u)$ versus the available experimental data. As seen from Table 10, the $\nu_1 + \nu_3$ and $\nu_1 + 3\nu_3$ combination bands reported by Smith et al.²⁶ at 2609.3 and 5517.2 cm^{-1} are predicted to appear at 2539.2(2563.3) and 5383.0(5441.0) cm^{-1} , respectively, from CHIPR (CHIPR-2BD-EXP). As previously noted and shown in Table 11, all Min(D_{3h})'s attributes calculated from the CHIPR-2BD-EXP form are in closer agreement with experiment than CHIPR; this can be further checked using the predicted B constants and electronic

term values T (with respect to ground-state C_3 PES of ref 14). The estimated \tilde{w}_2 value of 542.4 cm^{-1} matches the experimental unperturbed bending frequency $w_2 = 542.3 \text{ cm}^{-1}$ reported by Tokaryk et al.¹⁹

We now turn to the case of $C_3(^3A'_2)$. Although such species has not yet been detected, our best estimate places it 8002.3 cm^{-1} above the ground-vibronic state of $C_3(\tilde{\chi}^1\Sigma_g^+)$; see Table 11. As highlighted in the Introduction, this is therefore the first excited state of the carbon trimer. A major aspect on the $C_3(^3A'_2)$'s calculated spectrum, already remarked for⁸² cyclic $N_3^+(\tilde{\chi}^1A'_1)$, relates to the fact that, for a given v_1 and v_2 , the energies of the vibrational states (v_1, v_2^l) always drop as long as l increases (Table 9). For example, the (0,4⁴) level is found $\approx 50 \text{ cm}^{-1}$ below (0,4²) which, in turn, appears $\approx 20 \text{ cm}^{-1}$ lower in energy than (0,4⁰). As seen from Table 11, such a feature is clearly translated into the negative values of the l -dependent anharmonicity constant g_{22} in eq 19. From the above, and as suggested in ref 82, it appears that, unlike $C_3(\tilde{\alpha}^3\Pi_u)$, in $C_3(^3A'_2)$ the separate excitation of each degenerate component of w_2 (v_{2a} or v_{2b}) requires less energy than their simultaneous excitation.⁵³ Moreover, the calculated spectrum shows the lifting of non-genuine degenerate levels; e.g., it is seen that the $A'_2 + A'_1$ components of (0,3³) and (1,3³) are split by $\sim 3 \text{ cm}^{-1}$.

As Table 11 shows, $C_3(^3A'_2)$ is herein predicted to be an oblate symmetric top with rotational constants $A_0 = 0.74457$ and $B_0 = 1.49521 \text{ cm}^{-1}$. Note that A is associated with the rotational motion about the symmetry (figure) axis, while B to the other two mutually orthogonal and equal principal moments of inertia.⁵³ The corresponding vibrationally averaged (r_0) bond length is about 0.01 a_0 larger than the equilibrium r_e value. Although pure rotational spectra cannot arise due to zero dipole moment, rovibrational transitions are expected to occur in $C_3(^3A'_2)$ brought by its IR active pseudorotational motion. Our best estimate of the (central)

band origin is 1095.9 cm^{-1} (its A'_1 transition frequency of 1522.7 cm^{-1} is IR inactive).

6. CONCLUSIONS

We report the first global ab initio-based PES for ground-state triplet $C_3(^3A')$ based on accurate CBS extrapolated MRCI(Q) energies and the CHIPR method for analytical modeling. By relying on a cost-effective GUSTE(D,T) protocol, we ensure that the final form reproduces all topographical features of the PES, including its cyclic-linear isomerization barrier, with GUSTE(5,6)-quality. To partially account for the incompleteness of the N -electron basis and other minor effects, the available accurate experimental data on the relevant diatomics were used to obtain direct-fit curves, which replace the theoretical ones in the MBE series. Besides describing properly the long-range interactions at all asymptotic channels and the permutational symmetry by built-in construction (an asset already warranted by the purely ab initio form), the mixed theoretical/experimental PES, referred to as CHIPR-2BD-EXP, is shown to reproduce the proper exothermicities at dissociation regions, spectroscopy of the diatomic fragments and to slightly enhance the accuracy of the overall predicted attributes. Bound vibrational state calculations in both linear and cyclic isomers have also been carried out, unveiling a good match of the available data on $C_3(\tilde{\alpha}\ ^3\Pi_u)$ while providing accurate IR band positions for $C_3(^3A'_2)$ that may guide its laboratory and astronomical detection.

■ ASSOCIATED CONTENT

Supporting Information

The Supporting Information is available free of charge on the ACS Publications website at DOI: [10.1021/acs.jpca.9b03194](https://doi.org/10.1021/acs.jpca.9b03194).

Analytic gradients for a general CHIPR triatomic PES, extended versions of Tables 1 and 5, numerical coefficients of the final CHIPR form, ab initio data set as well as the parameters employed in the rovibrational DVR3D calculations ([PDF](#))

■ AUTHOR INFORMATION

Corresponding Author

*E-mail: varandas@uc.pt.

ORCID

C.M.R. Rocha: 0000-0002-4118-8308

A.J.C. Varandas: 0000-0003-1501-3317

Notes

The authors declare no competing financial interest.

■ ACKNOWLEDGMENTS

This work is supported by the Foundation for Science and Technology and Coimbra Chemistry Center, Portugal, in the framework of the project “MATIS—Materiais e Tecnologias Industriais Sustentáveis” (reference: CENTRO-01-0145-FEDER-000014), co-financed by the European Regional Development Fund (FEDER), through the “Programa Operacional Regional do Centro” (CENTRO2020) program. C.M.R.R. thanks also the CAPES Foundation (Ministry of Education of Brazil) for a scholarship (BEX 0417/13-0). A.J.C.V. thanks also the support from China’s Shandong Province “Double-Hundred Talent Plan” (2018).

■ REFERENCES

- (1) Van Orden, A.; Saykally, R. J. Small Carbon Clusters: Spectroscopy, Structure, and Energetics. *Chem. Rev.* **1998**, *98*, 2313–2358.
- (2) Varandas, A. J. C.; Rocha, C. M. R. C_n ($n = 2\text{-}4$): Current Status. *Philos. Trans. R. Soc., A* **2018**, *376*, No. 20170145.
- (3) Hargreaves, R. J.; Hinkle, K.; Bernath, P. F. Small Carbon Chains in Circumstellar Envelopes. *Mon. Not. R. Astron. Soc.* **2014**, *444*, 3721.
- (4) Lara, L. M.; Lin, Z.-Y.; Rodrigo, R.; Ip, W.-H. 67P/Churyumov-Gerasimenko Activity Evolution During its Last Perihelion before the Rosetta Encounter. *Astron. Astrophys.* **2011**, *525*, A36.
- (5) Cernicharo, J.; Goicoechea, J. R.; Caux, E. Far-Infrared Detection of C_3 in Sagittarius B2 and IRC+10216. *Astrophys. J.* **2000**, *534*, L199.
- (6) Mookerjea, B.; Hassel, G. E.; Gerin, M.; Giessen, T.; Stutzki, J.; Herbst, E.; Black, J. H.; Goldsmith, P. F.; Menten, K. M.; Krelowski, J.; et al. Chemistry of C_3 and Carbon Chain Molecules in DR21(OH). *Astron. Astrophys.* **2012**, *546*, A75.
- (7) Glinski, R. J.; Nuth, J. A. Can the Red Rectangle Molecular Emission Bands Be Assigned to C_3 ? *Astrophys. Space Sci.* **1997**, *249*, 143–149.
- (8) Wakelam, V.; Loison, J.-C.; Herbst, E.; Talbi, D.; Quan, D.; Caralp, F.; Sensitivity, A. A Sensitivity Study of the Neutral-Neutral Reactions $C+C_3$ and $C+C_5$ in Cold Dense Interstellar Clouds. *Astron. Astrophys.* **2009**, *495*, 513–521.
- (9) Loison, J.-C.; Wakelam, V.; Hickson, K. M.; Bergeat, A.; Mereau, R. The Gas-Phase Chemistry of Carbon Chains in Dark Cloud Chemical Models. *Mon. Not. R. Astron. Soc.* **2013**, *437*, 930–945.
- (10) Hébrard, E.; Dobrijevic, M.; Loison, J.-C.; Bergeat, A.; Hickson, K. M.; Caralp, F. Photochemistry of C_3H_p Hydrocarbons in Titan’s Stratosphere Revisited. *Astron. Astrophys.* **2013**, *552*, A132.
- (11) Venot, O.; Hébrard, E.; Agúndez, M.; Decin, L.; Bounaceur, R. New Chemical Scheme for Studying Carbon-Rich Exoplanet Atmospheres. *Astron. Astrophys.* **2015**, *577*, A33.
- (12) Leider, H.; Krikorian, O.; Young, D. Thermodynamic Properties of Carbon up to the Critical Point. *Carbon* **1973**, *11*, 555–563.
- (13) Goulay, F.; Nemes, L.; Schrader, P. E.; Michelsen, H. A. Spontaneous Emission From $C_2(d^3\Pi_g)$ and $C_3(A^1\Pi_u)$ During Laser Irradiation of Soot Particles. *Mol. Phys.* **2010**, *108*, 1013–1025.
- (14) Rocha, C. M. R.; Varandas, A. J. C. Energy-Switching Potential Energy Surface for Ground-State C_3 . *Chem. Phys. Lett.* **2018**, *700*, 36–43.
- (15) Murrell, J. N.; Carter, S.; Farantos, S. C.; Huxley, P.; Varandas, A. J. C. *Molecular Potential Energy Functions*; John Wiley & Sons: Chichester, 1984.
- (16) Jungen, C.; Merer, A. J. Orbital Angular Momentum in Triatomic Molecules. *Mol. Phys.* **1980**, *40*, 95–114.
- (17) Saha, S.; Western, C. M. Experimental and *Ab Initio* Study of a New $\tilde{D}^1\Delta_g$ State of the C_3 Radical. *J. Chem. Phys.* **2006**, *125*, No. 224307.
- (18) Tokaryk, D. W.; Civis, S. Infrared Emission Spectra of C_3 : The Renner Effect in the $\tilde{a}^3\Pi_u$ and $\tilde{b}^3\Pi_g$ Electronic States. *J. Chem. Phys.* **1995**, *103*, 3928–3941.
- (19) Tokaryk, D. W.; Harvie, D. J.; Lees, R. M.; Xu, L.-H. Bending Vibrational Wave Numbers in the $\tilde{a}^3\Pi_u$ and $\tilde{b}^3\Pi_g$ States of C_3 . *J. Chem. Phys.* **2002**, *117*, 4825–4830.
- (20) Rocha, C. M. R.; Varandas, A. J. C. The Jahn-Teller plus Pseudo-Jahn-Teller Vibronic Problem in the C_3 Radical and its Topological Implications. *J. Chem. Phys.* **2016**, *144*, No. 064309.
- (21) Rocha, C. M. R.; Varandas, A. J. C. Multiple Conical Intersections in Small Linear Parameter Jahn-Teller Systems: the DMBe Potential Energy Surface of Ground-State C_3 Revisited. *Phys. Chem. Chem. Phys.* **2018**, *20*, 10319–10331.
- (22) Rocha, C. M. R.; Varandas, A. J. C. Accurate *Ab Initio*-Based Double Many-Dody Expansion Potential Energy Surface for the Adiabatic Ground-State of the C_3 Radical Including Combined Jahn-Teller plus Pseudo-Jahn-Teller Interactions. *J. Chem. Phys.* **2015**, *143*, No. 074302.

- (23) Weltner, W.; McLeod, D. Spectroscopy of Carbon Vapor Condensed in Rare-Gas Matrices at 4 and 20 K. II. *J. Chem. Phys.* **1964**, *40*, 1305–1316.
- (24) Bondybey, V. E.; English, J. H. Relaxation Processes in Matrix Isolated C₃. *J. Chem. Phys.* **1978**, *68*, 4641–4643.
- (25) Sasada, H.; Amano, T.; Jarman, C.; Bernath, P. F. A New Triplet Band System of C₃: The $b^3\Pi_g$ - $\tilde{a}^3\Pi_u$ Transition. *J. Chem. Phys.* **1991**, *94*, 2401–2407.
- (26) Smith, A. M.; Agreiter, J.; Engel, C.; Bondybey, V. E. FT-IR Studies of Optically Pumped C₃ in Rare Gas Matrices. The Vibrational and Electronic Absorption Spectrum of the $\tilde{a}^3\Pi_u$ State. *Chem. Phys. Lett.* **1993**, *207*, 531–539.
- (27) Hwang, C.; Klassen, S.; Moazzen-Ahmadi, N.; Tokaryk, D. Infrared Diode Laser Spectroscopy of C₃: the ν_3 Band of the $\tilde{a}^3\Pi_u$ Electronic State. *Chem. Phys. Lett.* **1996**, *250*, 273–278.
- (28) Williams, G. R. J. The C₃ Radical: A Theoretical Study of the Electronic Spectrum of C₃ via the Equations of Motion Method. *Chem. Phys. Lett.* **1975**, *33*, 582–584.
- (29) Perić-Radić, J.; Römelt, J.; Peyerimhoff, S. D.; Buenker, R. J. Configuration Interaction Calculation of the Potential Curves for the C₃ Molecule in its Ground and Lowest-Lying Π_u States. *Chem. Phys. Lett.* **1977**, *50*, 344–350.
- (30) Whiteside, R. A.; Krishnan, R.; Frisch, M. J.; Pople, J. A.; Schleyer, P. V. R. Cyclic C₃ Structures. *Chem. Phys. Lett.* **1981**, *80*, 547–551.
- (31) Jones, R. O. Energy Surfaces of Low-Lying States of C₃. *J. Chem. Phys.* **1985**, *82*, 5078–5083.
- (32) Fueno, H.; Taniguchi, Y. *Ab Initio* Molecular Orbital Study of the Isomerization Reaction Surfaces of C₃ and C₃⁻. *Chem. Phys. Lett.* **1999**, *312*, 65–70.
- (33) Mebel, A. M.; Kaiser, R. I. An *Ab Initio* Study on the Formation of Interstellar Tricarbon Isomers l-C₃(X¹ Σ_g^+) and c-C₃(X³A₂). *Chem. Phys. Lett.* **2002**, *360*, 139–143.
- (34) Terentyev, A.; Scholz, R.; Schreiber, M.; Seifert, G. Theoretical Investigation of Excited States of C₃. *J. Chem. Phys.* **2004**, *121*, 5767–5776.
- (35) Sych, Y.; Bornhauser, P.; Knopp, G.; Liu, Y.; Gerber, T.; Marquardt, R.; Radi, P. P. Perturbation Facilitated Two-Color Four-Wave-Mixing Spectroscopy of C₃. *J. Chem. Phys.* **2013**, *139*, No. 154203.
- (36) Huang, W.-J.; Sun, Y.-L.; Chin, C.-H.; Lee, S.-H. Dynamics of the Reaction of C₃($\tilde{a}^3\Pi_u$) Radicals with C₂H₂: A New Source for the Formation of C₅H. *J. Chem. Phys.* **2014**, *141*, No. 124314.
- (37) Varandas, A. J. C. Combined-Hyperbolic-Inverse-Power-Representation of Potential Energy Surfaces: A Preliminary Assessment for H₃ and HO₂. *J. Chem. Phys.* **2013**, *138*, No. 054120.
- (38) Varandas, A. J. C. Accurate Combined-Hyperbolic-Inverse-Power-Representation of *Ab Initio* Potential Energy Surface for the Hydroperoxyl Radical and Dynamics Dtudy of O+OH Reaction. *J. Chem. Phys.* **2013**, *138*, No. 134117.
- (39) Varandas, A. J. C. In *Reaction Rate Constant Computations: Theories and Applications*; Han, K., Chu, T., Eds.; The Royal Society of Chemistry, 2013; Chapter 17, pp 408–445.
- (40) Szalay, P. G.; Müller, T.; Gidofalvi, G.; Lischka, H.; Shepard, R. Multiconfiguration Self-Consistent Field and Multireference Configuration Interaction Methods and Applications. *Chem. Rev.* **2012**, *112*, 108–181.
- (41) Dunning, T. H. Gaussian Basis Sets for Use in Correlated Molecular Calculations. I. The Atoms Boron through Neon and Hydrogen. *J. Chem. Phys.* **1989**, *90*, 1007–1023.
- (42) Kendall, R. A.; Dunning, T. H.; Harrison, R. J. Electron Affinities of the First-Row Atoms Revisited. Systematic Basis Sets and Wave Functions. *J. Chem. Phys.* **1992**, *96*, 6796–6806.
- (43) Werner, H. J.; Knowles, P. J.; Knizia, G.; Manby, F. R.; Schütz, M. et al. MOLPRO; a Package of *Ab Initio* Programs, version 2010.1; MOLPRO: Cardiff, U.K., 2010. see <http://www.molpro.net>.
- (44) Varandas, A. J. C. Straightening the Hierarchical Staircase for Basis Set Extrapolations: A Low-Cost Approach to High-Accuracy Computational Chemistry. *Annu. Rev. Chem.* **2018**, *69*, 177–203.
- (45) Varandas, A. J. C. Extrapolating to the One-Electron Basis-Set Limit in Electronic Structure Calculations. *J. Chem. Phys.* **2007**, *126*, No. 244105.
- (46) Pansini, F. N. N.; Neto, A. C.; Varandas, A. J. C. Extrapolation of Hartree-Fock and Multiconfiguration Self-Consistent-Field Energies to the Complete Basis Set Limit. *Theor. Chem. Acc.* **2016**, *135*, 261–267.
- (47) Varandas, A. J. C.; Pansini, F. N. N. Narrowing the Error in Electron Correlation Calculations by Basis Set Re-hierarchization and Use of the Unified Singlet and Triplet Electron-Pair Extrapolation Scheme: Application to a Test Set of 106 Systems. *J. Chem. Phys.* **2014**, *141*, No. 224113.
- (48) Pansini, F. N. N.; Neto, A. C.; Varandas, A. J. C. On the Performance of Various Hierarchized Bases in Extrapolating the Correlation Energy to the Complete Basis Set Limit. *Chem. Phys. Lett.* **2015**, *641*, 90–96.
- (49) Varandas, A. J. C. Generalized Uniform Singlet- and Triplet-Pair Extrapolation of the Correlation Energy to the One Electron Basis Set Limit. *J. Phys. Chem. A* **2008**, *112*, 1841–1850.
- (50) Varandas, A. J. C.; Piecuch, P. Extrapolating Potential Energy Surfaces by Scaling Electron Correlation at a Single Geometry. *Chem. Phys. Lett.* **2006**, *430*, 448–453.
- (51) Galvão, B. R. L.; Varandas, A. J. C. Accurate Double Many-Body Expansion Potential Energy Surface for N₃(⁴A^{''}) from Correlation Scaled *Ab Initio* Energies with Extrapolation to the Complete Basis Set Limit. *J. Phys. Chem. A* **2009**, *113*, 14424–14430.
- (52) Varandas, A. J. C. Intermolecular and Intramolecular Potentials: Topographical Aspects, Calculation, and Functional Representation via A Double Many-Body Expansion Method. *Adv. Chem. Phys.* **1988**, *74*, 255–338.
- (53) Herzberg, G. *Molecular Spectra and Molecular Structure III. Electronic Spectra and Electronic Structure of Polyatomic Molecules*; Van Nostrand: New York, 1966.
- (54) Mota, V. C.; Varandas, A. J. C. HN₂(²A[']) Electronic Manifold. II. *Ab Initio* Based Double-Sheeted DMBE Potential Energy Surface via a Global Diabatization Angle. *J. Phys. Chem. A* **2008**, *112*, 3768–3786.
- (55) Varandas, A. J. C. Extrapolation to the Complete-Basis-Set Limit and the Implications of Avoided Crossings: The X¹ Σ_g^+ , B¹ Δ_g and B'¹ Σ_g^+ States of C₂. *J. Chem. Phys.* **2008**, *129*, No. 234103.
- (56) Varandas, A. J. C. A Simple, Yet Reliable, Direct Diabatization Scheme. The ¹ Σ_g^+ States of C₂. *Chem. Phys. Lett.* **2009**, *471*, 315–321.
- (57) Varandas, A. J. C. Accurate *Ab Initio* Potential Energy Curves for the Classic Li-F Ionic-Covalent Interaction by Extrapolation to the Complete Basis Set Limit and Modeling of the Radial Nonadiabatic Coupling. *J. Chem. Phys.* **2009**, *131*, No. 124128.
- (58) Golub, G. H.; Van der Vorst, H. A. Eigenvalue Computation in the 20th Century. *J. Comput. Appl. Math.* **2000**, *123*, 35–65.
- (59) Levenberg, K. A Method for the Solution of Certain Problems in Least Squares. *Q. Appl. Math.* **1944**, *2*, 164–168.
- (60) Marquardt, D. W. An Algorithm for Least-Squares Estimation of Nonlinear Parameters. *J. Soc. Ind. Appl. Math.* **1963**, *11*, 431–441.
- (61) Press, W. H.; Teukolsky, S. A.; Vetterling, W. T.; Flannery, B. P. *Numerical Recipes in Fortran: The Art of Scientific Computing*, 2nd ed.; Cambridge University Press: New York, 1993.
- (62) Chen, W.; Kawaguchi, K.; Bernath, P. F.; Tang, J. Simultaneous Analysis of the Ballik-Ramsay and Phillips Systems of C₂ and Observation of Forbidden Transitions Between Singlet and Triplet States. *J. Chem. Phys.* **2015**, *142*, No. 064317.
- (63) Urdahl, R. S.; Bao, Y.; Jackson, W. M. An Experimental Determination of the Heat of Formation of C₂ and the C-H Bond Dissociation Energy in C₂H. *Chem. Phys. Lett.* **1991**, *178*, 425–428.
- (64) Schmidt, T. W.; Bacsay, G. B. Oscillator Strengths of the Mulliken, Swan, Ballik-Ramsay, Phillips, and d³ Π_g -c³ Σ_u^+ Systems of C₂ Calculated by MRCI Methods Utilizing a Biorthogonal Transformation of CASSCF Orbitals. *J. Chem. Phys.* **2007**, *127*, No. 234310.
- (65) Boggio-Pasqua, M.; Voronin, A. I.; Halvick, P.; Rayez, J. C. Analytical Representations of High Level *Ab Initio* Potential Energy

Curves of the C₂ Molecule. *J. Mol. Struct.: THEOCHEM* **2000**, *531*, 159–167.

(66) Yurchenko, S. N.; Szabó, I.; Pyatenko, E.; Tennyson, J. ExoMol Line Lists XXXI: Spectroscopy of Lowest Eight Electronic States of C₂. *Mon. Not. R. Astron. Soc.* **2018**, *480*, 3397–3411.

(67) Le Roy, R. J. LEVEL: A Computer Program for Solving the Radial Schrödinger Equation for Bound and Quasibound Levels. *J. Quant. Spectrosc. Radiat. Transfer* **2017**, *186*, 167–178.

(68) Varandas, A. J. C.; Rodrigues, S. P. J.; Batista, V. M. O. Direct Fit of Extended Hartree-Fock Approximate Correlation Energy Model to Spectroscopic Data. *Chem. Phys. Lett.* **2006**, *424*, 425–431.

(69) Xavier, F. G. D.; Martínez-González, M.; Varandas, A. J. C. Accurate *Ab Initio* Potential for HO₂⁺: CBS Extrapolated Energies and Direct-Fit Diatomic Curves. *Chem. Phys. Lett.* **2018**, *691*, 421–430.

(70) Varandas, A. J. C.; Galvão, B. R. L. Exploring the Utility of Many-Body Expansions: A Consistent Set of Accurate Potentials for the Lowest Quartet and Doublet States of the Azide Radical with Revisited Dynamics. *J. Phys. Chem. A* **2014**, *118*, 10127–10133.

(71) Sagan, B. E. *The Symmetric Group: Representations, Combinatorial Algorithms, and Symmetric Functions*, 2nd ed.; Springer: New York, 2001.

(72) Braams, B. J.; Bowman, J. M. Permutationally Invariant Potential Energy Surfaces in High Dimensionality. *Int. Rev. Phys. Chem.* **2009**, *28*, 577–606.

(73) Xie, Z.; Bowman, J. M. Permutationally Invariant Polynomial Basis for Molecular Energy Surface Fitting via Monomial Symmetrization. *J. Chem. Theory Comput.* **2010**, *6*, 26–34.

(74) Ayouz, M.; Babikov, D. Improved Potential Energy Surface of Ozone Constructed Using the Fitting by Permutationally Invariant Polynomial Function. *Adv. Phys. Chem.* **2012**, *2012*, No. 951371.

(75) Ayouz, M.; Babikov, D. Global Permutationally Invariant Potential Energy Surface for Ozone Forming Reaction. *J. Chem. Phys.* **2013**, *138*, No. 164311.

(76) Varandas, A. J. C. A Useful Triangular Plot of Triatomic Potential Energy Surfaces. *Chem. Phys. Lett.* **1987**, *138*, 455–461.

(77) Tennyson, J.; Kostin, M. A.; Barletta, P.; Harris, G. J.; Polyansky, O. L.; Ramanlal, J.; Zobov, N. F. DVR3D: A Program Suite for the Calculation of Rotation-Vibration Spectra of Triatomic Molecules. *Comput. Phys. Commun.* **2004**, *163*, 85–116.

(78) Pople, J. A. The Renner Effect and Spin-Orbit Coupling. *Mol. Phys.* **1960**, *3*, 16–22.

(79) Carter, S.; Handy, N. C. A Variational Method for the Calculation of Ro-Vibronic Levels of Any Orbitally Degenerate (Renner-Teller) Triatomic Molecule. *Mol. Phys.* **1984**, *52*, 1367–1391.

(80) Izuha, M.; Yamanouchi, K. J. New $\tilde{A}-\tilde{X}$ Vibronic Bands of Laser-Vaporized C₃. *Chem. Phys.* **1998**, *109*, 1810–1818.

(81) Sutcliffe, B. T.; Tennyson, J. A Generalized Approach to the Calculation of Ro-Vibrational Spectra of Triatomic Molecules. *Mol. Phys.* **1986**, *58*, 1053–1066.

(82) Babikov, D.; Mozhayskiy, V. A.; Krylov, A. I. The Photo-electron Spectrum of Elusive Cyclic-N₃ and Characterization of the Potential Energy Surface and Vibrational States of the Ion. *J. Chem. Phys.* **2006**, *125*, No. 084306.